

Copyright © 1985, by the author(s).
All rights reserved.

Permission to make digital or hard copies of all or part of this work for personal or classroom use is granted without fee provided that copies are not made or distributed for profit or commercial advantage and that copies bear this notice and the full citation on the first page. To copy otherwise, to republish, to post on servers or to redistribute to lists, requires prior specific permission.

POINT-MATCHED TIME DOMAIN FINITE ELEMENT METHODS
FOR ELECTROMAGNETIC RADIATION AND SCATTERINGS

by

A. C. Cangellaris, C. C. Lin, K. K. Mei

Memorandum No. UCB/ERL M85/25

11 April 1985

COVER PAGE

POINT-MATCHED TIME DOMAIN FINITE ELEMENT METHODS
FOR ELECTROMAGNETIC RADIATION AND SCATTERINGS

by

A. C. Cangellaris, C. C. Lin, K. K. Mei

Memorandum No. UCB/ERL M85/25

11 April 1985

ELECTRONICS RESEARCH LABORATORY

College of Engineering
University of California, Berkeley
94720

Title Page

Point-Matched Time Domain Finite Element
Methods for Electromagnetic Radiation and Scattering*

A. C. Cangellaris, C. C. Lin and K. K. Mei

Department of Electrical Engineering and Computer Sciences
and the Electronics Research Laboratory
University of California, Berkeley, CA 94720

Abstract

Direct time domain computation of Maxwell's differential equations will soon become a practical technique because of the availability of super-computers. This paper presents the principle methods used in time domain computations and the supporting theories. The Point-Matched finite element method is chosen as the main feature of this presentation, which includes the discretization of equations, conforming mesh generation, dielectric and metallic interfaces, numerical stability and simulation of radiation conditions. Numerical results of scattering of Gaussian pulses are presented in time sequences.

* Research sponsored by the Army Research Office Contract DAAG29-84-K-0067 and the Office of Naval Research Contract N00014-84-K-0272.

1. Introduction

The art of computation in electromagnetic wave scattering and radiation has a recent history of two decades. Traditionally, wave scattering computations are done in frequency domain, and it is now a mature technology lending its application to many branches of electromagnetic discipline. Time domain computation on the other hand is still a novelty, which has been reported [1]-[4] but not been taken seriously by the electromagnetic community. This situation may soon change, because the new generation of computers, with the vast memory capacities, can be most effectively applied if the algorithm makes use of the memory in a simple sequential order. Time domain computations of Maxwell's equations in differential form appear to use that type of algorithm. Furthermore, it is much easier to get frequency domain results from time domain data, than the other way around, hence it is often more economical to get frequency domain results via time domain if many frequencies are involved. Although time domain computation will not replace frequency domain computation in most applications, it will definitely break new grounds in inhomogeneous media and non-linear computations. In the area of scattering by large arbitrary shaped three dimensional targets, the time domain computation will definitely be a strong contender to the more established frequency domain methods.

Time domain computation using finite difference equations was first presented by Yee [1] in 2-dimensions and later applied to 3-dimensions by Kunz and Lee [2] and Taflov and Brodwin [4]. The improvement to conforming meshes was done by Cangellaris et al. [5], and extension to lossy environment by Lin and Mei [6].

The purpose of this paper is to present the principal techniques used in time domain computations and the supporting theories so that an uninitiated reader may quickly learn to apply the methods. We have chosen the Point-

matched Time Domain Finite Element Method as the principal feature of this paper because it appears to be more general than the finite difference methods, and because the important issue of conforming mesh was not properly addressed in finite difference methods.

Included in this paper are topics on discretization of Maxwell's equations, conforming mesh generation, dielectric and metal interfaces, numerical stability and simulation of radiation conditions. Each of these topics becomes more and more complex as the space dimension of the problem increases. Hence, for pedagogical reasons, we have organized this paper in increasing order of space dimensions. Illustrative results are presented in one and two space dimensions only, because at the time of writing, a general 3-dimensional code is still being implemented. And, also a three dimensional problem is sufficiently complex that a separate treatise is in order.

The main theme of this paper is the unfoldment of the space and time history of an electromagnetic event. Indeed, this idea of predicting the future by studying the past and current event is as old as Confucius, who said

"From the knowledge of one corner, he (a good student)
finds those of the other three,
By studying the past, he (a good teacher)
predicts the future"*

2.1. Basics

The phenomena of electromagnetic radiation and scattering are completely known if the associated wave equations can be solved. The goal of this section is to present the basic framework of the point-matched time domain finite-element method as an efficient technique of solving such equations. For tutorial

* Paraphrased from Analecta of Confucius.

purpose, we start our discussion with a simple one-dimensional problem.

Maxwell's equations, reduced to one space dimension may be represented by a first order linear hyperbolic system,

$$\frac{\partial}{\partial t} \begin{bmatrix} E_x \\ H_y \end{bmatrix} = \begin{bmatrix} 0 & -\frac{1}{\epsilon_0} \\ -\frac{1}{\mu_0} & 0 \end{bmatrix} \frac{\partial}{\partial z} \begin{bmatrix} E_x \\ H_y \end{bmatrix} \quad (2.1)$$

where the subscripts x and y designate the components along \hat{x} and \hat{y} directions, respectively, of the vector fields. Upon substitution of the dependent variables, (2.1) can be replaced by a second order differential equation,

$$\left(\frac{\partial^2}{\partial z^2} - \mu_0 \epsilon_0 \frac{\partial^2}{\partial t^2} \right) \begin{bmatrix} E_x \\ H_y \end{bmatrix} = 0 \quad (2.2)$$

The velocity of propagation is $c = \frac{1}{\sqrt{\mu_0 \epsilon_0}}$.

Equations (2.1) and (2.2) are hyperbolic differential equations, which must satisfy specific initial and boundary conditions for unique solutions [7]. The initial and boundary conditions for the one-space-dimensional equations of (2.1), depicted in Fig. 2.1, can be summarized as follows:

- (1) The source in D must be known for all $t \geq 0$.
- (2) The initial state at $t = 0$, must be known everywhere in D , i.e., $E_x(z, 0)$ and $H_y(z, 0)$ are given.
- (3) The boundary conditions at B are specified at all times, i.e., $E_x(0, t)$ or $H_y(0, t)$ on the left, and $E_x(L, t)$ or $H_y(L, t)$ on the right boundary.

Numerical solutions of Eq. (2.1) or (2.2) start with the discretization of D into finite subsegments. For the convenience of enforcing the initial conditions at $t = 0$, it is often preferable to solve Eq. (2.1) rather than (2.2), even though two dependent variables are involved in (2.1). The coupling of E_x and H_y in (2.1) suggests a space discretization scheme as shown in Fig. 2.2 where the nodes of

E_{x_i} and H_{y_i} are offset by one half step, and a similar discretization in time, where E_{x_i} are computed at temporal nodes $t = n\Delta t$ and H_{y_i} at $t = (n + \frac{1}{2})\Delta t$ where $n = 1, 2, \dots$. For convenience the fields at the nodes are denoted by E_i^n and $H_i^{n+\frac{1}{2}}$ for $E_x[(i-1)\Delta z, n\Delta t]$ and $H_y[(i-\frac{1}{2})\Delta z, (n + \frac{1}{2})\Delta t]$ respectively. With this discretization scheme, commonly known as the Leap-Frog method, the finite-difference representation of (2.1) becomes,

$$\left\{ \begin{array}{l} \frac{E_i^n - E_i^{n-1}}{\Delta t} = -\frac{1}{\epsilon_0} \frac{H_i^{n-\frac{1}{2}} - H_{i-1}^{n-\frac{1}{2}}}{\Delta z} \\ \frac{H_i^{n+\frac{1}{2}} - H_i^{n-\frac{1}{2}}}{\Delta t} = -\frac{1}{\mu_0} \frac{E_{i+1}^n - E_i^n}{\Delta z} \end{array} \right. \quad (2.3)$$

It is apparent from (2.3) that E_i^n may be obtained from earlier electric and magnetic fields, and similarly for $H_i^{n+\frac{1}{2}}$. Assuming the system to be relaxed for $t < 0$, Eq. (2.3) can be computed sequentially with $n = 1, 2, \dots$, with the equations for E and H applied alternatively.

Equations (2.3) can be easily applied, even on a microcomputer. Figure 2.3a shows a Gaussian pulse launched from the left boundary and reflected back at the right boundary where the electric field is enforced to be zero for all time (perfectly conducting wall). On the other hand, the effect of a dielectric interface normal to the plane wave incidence is depicted in Fig. 2.3b: the reflection and transmission of the incident pulse due to the relative permittivity contrast ($\epsilon_r = 4$) is well demonstrated. The final example (Fig. 2.3c) illustrates the simulation of wave propagation in a semi-infinite region extending to the positive z direction. In this case, the boundary value $E(L, t)$ must be extrapolated from the interior solution:

$$E(L,t) = E(L-\Delta z, t - \frac{\Delta z}{c}) \quad (2.4)$$

The above technique effectively creates a reflection-less boundary (radiation or absorbing boundary) owing to the fact that we know the general solution for a right propagating wave:

$$f^+(z,t) = f(t - \frac{z}{c}) \quad (2.5)$$

Simple as it is, there are two issues in the computation of (2.1) which must be mentioned here, namely, the ratio $\frac{\Delta z}{\Delta t} \geq c$ must be enforced everywhere, and for infinite or semi-infinite region D , an artificial boundary at a finite distance must simulate an outgoing wave. The first condition affects the stability of solutions, and the second condition causes unwanted reflection or instability at the fictitious boundary. Those conditions are easily satisfied in this one-dimensional problem, but they are subjects of great concern in higher dimensions.

2.2. Point-Matching Finite-Element Method

Point-matching finite-element method [5] applied to Eq. (2.1) will also result in those of (2.3). Indeed, in one space dimension, the difference between the two methods is only in the approach rather than the resulting equations. We shall use the one-dimensional problem to introduce the technique as a vehicle to higher dimensional finite-element methods.

In finite element the fields are not only defined at the nodes, but are also defined in the space between nodes. The space between two adjacent nodes is called an element. The elements for E_x and H_y , which are offset as before, shown in Fig. 2.2, form two complementary sets of nodal points. All elements sharing a common node form a support for a trial or basis function. The trial

function is called interpolative if its value is unity at the common node and zero at all other nodes. The simplest interpolative functions are linear functions. In one space dimension the linear interpolative basis functions are shown in Fig. 2.4. In two space dimensions, linear interpolative functions are applicable for triangular elements; bilinear interpolative functions may be used for rectangular elements [8]. Using the basis functions $\varphi_i(z)$ and $\psi_i(z)$ for E_x and H_y (Fig. 2.5) respectively, we may represent the fields in product solutions,

$$\begin{cases} E_x(z, t) \cong \sum_{i=1}^M \varphi_i(z) E_{xi}(t) \\ H_y(z, t) \cong \sum_{i=1}^{M-1} \psi_i(z) H_{yi}(t) \end{cases} \quad (2.6)$$

Substitution of (2.6) into (2.1) results in

$$\begin{cases} \sum_{i=1}^M \varphi_i(z) \frac{dE_{xi}(t)}{dt} = -\frac{1}{\epsilon_0} \sum_{i=1}^{M-1} \frac{d\psi_i(z)}{dz} H_{yi}(t) \\ \sum_{i=1}^{M-1} \psi_i(z) \frac{dH_{yi}(t)}{dt} = -\frac{1}{\mu_0} \sum_{i=1}^M \frac{d\varphi_i(z)}{dz} E_{xi}(t) \end{cases} \quad (2.7)$$

where

$$\varphi_i(z) = \begin{cases} 1 - \frac{|z_i - z|}{\Delta z}, & z_{i-1} \leq z \leq z_{i+1} \\ 0, & \text{otherwise} \end{cases}$$

$$\psi_i(z) = \begin{cases} 1 - \frac{|z'_i - z|}{\Delta z}, & z'_{i-1} \leq z \leq z'_{i+1} \\ 0, & \text{otherwise} \end{cases}$$

where z_i and z'_i are offset by $\frac{\Delta z}{2}$.

If (2.7) are equated at each nodal point and the "Leap-Frog" finite-difference method [9] is applied for the temporal variable t , we obtain the equa-

tions for point-matching finite-element method which are identical to equations for E_{xi}^n and $H_{yi}^{n+\frac{1}{2}}$ in (2.3). Equations (2.7) are more general than (2.3) in that the equality of the approximate representations can be defined in terms of weighting functions, i.e., both sides are multiplied by a weighting function $\omega_j(z)$ and the products are integrated in region D . The resulting equations will have the form,

$$\begin{aligned} [K_{\dot{E}}][\dot{E}_x] &= [K_H][H_y] \\ [K_{\dot{H}}][\dot{H}_y] &= [K_E][E_x] \end{aligned} \quad (2.8)$$

where $K_{\dot{E}}$, $K_{\dot{H}}$, K_H and K_E are matrices, E_x, H_y are vectors of the nodal values of E_{xi}, H_{yi} . In general the $K_{\dot{E}}$ and $K_{\dot{H}}$ matrices are diagonal only when the weighting functions are Dirac delta functions, i.e., point-matching. Hence no matrix inversion is required prior to the integration of (2.8).

The above described Leap-Frog scheme is not the only possible time discretization method. In fact, the restriction on the time increment size $\Delta t \leq \frac{\Delta z}{c}$ can be removed using implicit integration schemes [10] such as "trapezoidal rule":

$$\begin{cases} \frac{E_i^{n+1} - E_i^n}{\Delta t} = -\frac{1}{\epsilon_0} \frac{H_i^{n+1} + H_i^n - H_{i-1}^{n+1} - H_{i-1}^n}{2\Delta z} \\ \frac{H_i^{n+1} - H_i^n}{\Delta t} = -\frac{1}{\mu_0} \frac{E_{i+1}^{n+1} + E_{i+1}^n - E_i^{n+1} - E_i^n}{2\Delta z} \end{cases} \quad (2.9)$$

or "Backward difference scheme":

$$\begin{cases} \frac{E_i^{n+1} - E_i^n}{\Delta t} = -\frac{1}{\epsilon_0} \frac{H_i^{n+1} - H_{i-1}^{n+1}}{\Delta z} \\ \frac{H_i^{n+1} - H_i^n}{\Delta t} = -\frac{1}{\mu_0} \frac{E_{i+1}^{n+1} - E_i^{n+1}}{\Delta z} \end{cases} \quad (2.10)$$

This latter algorithm is especially popular among circuit analysts [11]. The price we have to pay for a better solution stability is that the future values E_i^{n+1} and H_i^{n+1} are now linearly coupled. However the matrix inversion can be avoided by taking advantage of the contraction mapping property of the above equations.

3.1. Finite-Difference and Finite-Element Methods.

As the dimensions of the problem increase, the differences between finite-difference and finite-element methods become more apparent. The finite-element mesh that is used over the computational domain consists of elements that conform to the contour of the body allowing the simulation of geometries with curved boundaries. Finite-difference methods on the other hand are restricted to a rectangular grid which approximates a curved boundary with discretely stepped surfaces.

Let us consider for example the problem of scattering by an infinite conducting cylinder. Without loss of generality we shall consider the case of an incident plane wave pulse with the electric field vector in the direction of the axis of the cylinder. The direction of incidence is \vec{k} as shown in Fig. 3.1. The Maxwell's equations to be solved are:

$$\frac{\partial H_x}{\partial t} = -\frac{1}{\mu} \frac{\partial E_z}{\partial y} \quad (3.1a)$$

$$\frac{\partial H_y}{\partial t} = \frac{1}{\mu} \frac{\partial E_z}{\partial x} \quad (3.1b)$$

$$\frac{\partial E_z}{\partial t} = \frac{1}{\epsilon} \left(\frac{\partial H_y}{\partial x} - \frac{\partial H_x}{\partial y} \right) \quad (3.1c)$$

In order to solve the above system of equations, the time domain finite difference method [1], [12]-[15] uses a stepped approximation of the circular boundary as shown in Fig. 3.2. In the same figure is also shown enlarged the

right rectangular mesh used for the space discretization of the electric and magnetic fields. The components of the electric and magnetic fields are discretized in time in equal intervals Δt , with the temporal nodes of H between those of E . For example, $E_z^n(i + \frac{1}{2}, j + \frac{1}{2})$ represents $E_z \left\{ (i + \frac{1}{2})h, (j + \frac{1}{2})h; n\Delta t \right\}$ for $n = 0, 1, 2, \dots$, and $H_x^{n+\frac{1}{2}}(i + \frac{1}{2}, j)$ represents $H_x \left\{ (i + \frac{1}{2})h, jh; (n + \frac{1}{2})\Delta t \right\}$, where h is the space increment for the lattice $h = \Delta x = \Delta y$. Thus \bar{E} is computed only at $t = 0, \Delta t, 2\Delta t, \dots$ and \bar{H} is computed only at $t = \frac{1}{2}\Delta t, (1 + \frac{1}{2})\Delta t, (2 + \frac{1}{2})\Delta t, \dots$. This lattice scheme in space and time plus the incident fields and boundary conditions result in a time marching algorithm. Since the tangential component of the electric field is zero on the scatterer, the scattered electric field is known as a function of time on the surface of the body. Therefore we can update the scattered fields on the grid by using the following finite difference approximations of (3.1)

$$H_x^{n+\frac{1}{2}}(i + \frac{1}{2}, j) = H_x^{n-\frac{1}{2}}(i + \frac{1}{2}, j) - \frac{\Delta t}{\mu h} \left\{ E_z^n(i + \frac{1}{2}, j + \frac{1}{2}) - E_z^n(i + \frac{1}{2}, j - \frac{1}{2}) \right\} \quad (3.2a)$$

$$H_y^{n+\frac{1}{2}}(i, j) = H_y^{n-\frac{1}{2}}(i, j) + \frac{\Delta t}{\mu h} \left\{ E_z^n(i + \frac{1}{2}, j + \frac{1}{2}) - E_z^n(i - \frac{1}{2}, j + \frac{1}{2}) \right\} \quad (3.2b)$$

$$E_z^{n+1}(i + \frac{1}{2}, j + \frac{1}{2}) = E_z^n(i + \frac{1}{2}, j + \frac{1}{2}) + \frac{\Delta t}{\epsilon h} \left\{ H_y^{n+\frac{1}{2}}(i+1, j + \frac{1}{2}) - H_y^{n+\frac{1}{2}}(i, j + \frac{1}{2}) - H_x^{n+\frac{1}{2}}(i + \frac{1}{2}, j+1) + H_x^{n+\frac{1}{2}}(i + \frac{1}{2}, j) \right\} \quad (3.2c)$$

The way the algorithm works is now apparent. Knowledge of the magnetic field at $t = (n + \frac{1}{2})\Delta t$ on the nodes surrounding the one where the electric field is computed together with the value of the electric field at $t = n \cdot \Delta t$ permits the computation of the electric field at $t = (n+1) \cdot \Delta t$. We see therefore that we can solve the transient problem using very simple arithmetic operations avoiding matrix inversion. But the *TDFD* has the disadvantage that, since the computational meshes are rectangular in shape, they do not conform to scatterers with smoothly curved surfaces. To overcome this problem one apparently has to use finite elements.

A finite element mesh for the 2-D conducting cylinder is shown in Fig. 3.3. One can see that the surface of the body is no longer approximated by the discretely stepped surfaces that appear in the finite difference formulation. Our task is to introduce a discretization of the Maxwell's equations in space and time, in such a way that the simple algorithm of the *TDFD* scheme is preserved.

As in Section 2.2, we assume that \bar{E} and \bar{H} can be written in the general functional forms:

$$\bar{E}(\bar{r}, t) \cong \sum_{i=1}^M \varphi_i(\bar{r}) \bar{E}_i(t) \quad (3.3)$$

$$\bar{H}(\bar{r}, t) \cong \sum_{j=1}^N \psi_j(\bar{r}) \bar{H}_j(t) \quad (3.4)$$

In contrast with the *TDFD* method this scheme positions all the components of the electric field on the same node. Similarly, for the magnetic field. On the other hand the interpolation functions $\varphi_i(\bar{r})$ and $\psi_j(\bar{r})$ allow us to describe any desirable variation of the fields within the elements while the *TDFD* method allows only a linear one. An example of $\varphi_i(\bar{r})$ in two dimensions is presented in Fig. 3.4a. It is centered on the i node and has four quadrilateral elements as support. It is obvious that the field within an element is represented as a linear

combination of the interpolation functions associated with its nodes as illustrated in Fig. 3.4b. This point will become important when we convert the summations (3.3) and (3.4) into other summations over the nodes of each element in order to express the internal field values. Although our formulation will be in terms of cartesian coordinates we must realize that sometimes it is preferable to use cylindrical or spherical coordinates. Our discretized Maxwell's equations will have sufficiently general forms such that a conversion to another coordinate system will be straightforward. We assume that the medium is isotropic. Maxwell's equations are then written as:

$$\nabla \times \bar{E} = -\mu \frac{\partial \bar{H}}{\partial t} \quad (3.5)$$

$$\nabla \times \bar{H} = \sigma \bar{E} + \varepsilon \frac{\partial \bar{E}}{\partial t} \quad (3.6)$$

For the sake of simplicity we shall neglect the conduction current. It is an easy task to reinsert the above term in the appropriate equation. The dielectric permittivity and the magnetic permeability of the medium are allowed to be continuous functions of position as well as functions of the electric and the magnetic field, respectively, in the non-linear case. Substitution of the general functional forms (3.3) and (3.4) into (3.5) and (3.6) yields:

$$\sum_{j=1}^N \psi_j(\bar{r}) \frac{dH_j(t)}{dt} = -\frac{1}{\mu} \sum_{i=1}^M \nabla \varphi_i(\bar{r}) \times \bar{E}_i(t) \quad (3.7)$$

$$\sum_{i=1}^M \varphi_i(\bar{r}) \frac{d\bar{E}_i(t)}{dt} = \frac{1}{\varepsilon} \sum_{j=1}^N \nabla \psi_j(\bar{r}) \times \bar{H}_j(t) \quad (3.8)$$

Since φ_i 's and ψ_j 's are known functions of position, the only unknowns in the above equations are the nodal values of the electric and magnetic field $\bar{E}_i(t)$ and $\bar{H}_j(t)$, where:

$$\bar{E}_i(t) = \{0, 0, E_{iz}(t)\}^T \quad i = 1, 2, \dots, M \quad (3.9)$$

$$\bar{H}_j(t) = \{H_{jx}(t), H_{jy}(t), 0\}^T \quad j = 1, 2, \dots, N \quad (3.10)$$

In order to obtain the weak forms of Maxwell's equations we enforce the above equations (3.7) and (3.8) on each nodal point. Since $\varphi_i(\bar{r})$ and $\psi_j(\bar{r})$ are defined to be

$$\varphi_i(\bar{r}) = \begin{cases} 1, & \bar{r} = \bar{r}_i \\ 0, & \text{on other nodes,} \end{cases} \quad \psi_j(\bar{r}) = \begin{cases} 1, & \bar{r} = \bar{r}_j \\ 0, & \text{on other nodes} \end{cases} \quad (3.11)$$

we obtain

$$\frac{d\bar{H}_j(t)}{dt} = -\frac{1}{\mu(\bar{r}_j)} \sum_{i=1}^M \nabla\varphi_i(\bar{r}_j) \times \bar{E}_i(t), \quad j = 1, 2, \dots, N \quad (3.12)$$

$$\frac{d\bar{E}_i(t)}{dt} = \frac{1}{\varepsilon(\bar{r}_i)} \sum_{j=1}^N \nabla\psi_j(\bar{r}_i) \times \bar{H}_j(t), \quad i = 1, 2, \dots, M \quad (3.13)$$

where for simplicity the notations

$$\nabla\varphi_i(\bar{r})|_{\bar{r}=\bar{r}_j} = \nabla\varphi_i(\bar{r}_j) \quad (3.14a)$$

$$\nabla\psi_j(\bar{r})|_{\bar{r}=\bar{r}_i} = \nabla\psi_j(\bar{r}_i) \quad (3.14b)$$

have been used.

Since φ_i 's and ψ_j 's have finite support in space it is clear that only a few terms in the summations will contribute. For example, if electric and magnetic nodes coincide, we see from Fig. 3.4a that only nine magnetic nodes will contribute to the computation of an electric node.

Although the use of a single mesh seems attractive it turns out that for the simplicity of the computation it is preferable to distribute the electric and magnetic nodes in such a way that they are mutually interspaced. An example of such a layout in two-dimensional space is presented in Fig.3.5. The electric and

magnetic fields are defined on two complementary grids such that the nodes of the former are positioned inside the elements of the latter. It is now obvious from Figs. 3.4 and 3.5 that only the interpolation functions associated with the nodes 1, 2, 3 and 4 in Fig. 3.5 will contribute to the summation in (3.12) for the point \bar{r}_j . In general if the element has K nodes, equations (3.12) and (3.13) become

$$\frac{d\bar{H}_j(t)}{dt} = -\frac{1}{\mu(\bar{r}_j)} \sum_{l=1}^K \nabla\varphi_l(\bar{r}_j) \times \bar{E}_l(t), \quad j = 1, 2, \dots, N \quad (3.15)$$

$$\frac{d\bar{E}_i(t)}{dt} = \frac{1}{\varepsilon(\bar{r}_i)} \sum_{l=1}^K \nabla\psi_l(\bar{r}_i) \times \bar{H}_l(t), \quad i = 1, 2, \dots, M \quad (3.16)$$

where it is understood that the summation on the right-hand side is carried out over the element enclosing the \bar{H} -field node \bar{r}_j for (3.15) or the \bar{E} -field node \bar{r}_i for (3.16).

Expanding equations (3.15) and (3.16) into component form, we get

$$\frac{dH_{jx}(t)}{dt} = -\frac{1}{\mu(\bar{r}_j)} \sum_{l=1}^K \left[\frac{\partial\varphi_l}{\partial y} \right]_{\bar{r}=\bar{r}_j} E_{lx}(t), \quad j = 1, 2, \dots, N \quad (3.17a)$$

$$\frac{dH_{jy}(t)}{dt} = \frac{1}{\mu(\bar{r}_j)} \sum_{l=1}^K \left[\frac{\partial\varphi_l}{\partial x} \right]_{\bar{r}=\bar{r}_j} E_{lx}(t), \quad j = 1, 2, \dots, N \quad (3.17b)$$

$$\frac{dE_{ix}(t)}{dt} = \frac{1}{\varepsilon(\bar{r}_i)} \sum_{l=1}^K \left\{ \left[\frac{\partial\psi_l}{\partial x} \right]_{\bar{r}=\bar{r}_i} H_{ly}(t) - \left[\frac{\partial\psi_l}{\partial y} \right]_{\bar{r}=\bar{r}_i} H_{lx}(t) \right\}, \quad (3.17c)$$

$$i = 1, 2, \dots, M$$

It is apparent that the convenient leap-frog scheme that was used in the *TDFD* method can also be implemented here for the time integration of the above system of equations. The finite element formulation succeeds in maintaining the simplicity of the *TDFD* method while being able to simulate any desirable geometry.

3.2. Two-Dimensional Elements

Before being able to conclude the solution of the 2-D problem of the last section we must discuss the choice of the interpolation functions $\varphi_i(\bar{r})$ and $\psi_j(\bar{r})$ together with the type of the elements and the different ways of generating the finite element mesh.

The choice of the type of element and the type of the interpolation function associated with it, is the key to every finite element modeling. It is well known that in order to guarantee convergence of our approximate solution to the correct one, the interpolation functions are required to satisfy the following conditions [16]:

1. At element interfaces the field variable and any of its partial derivatives up to one order less than the highest-order derivative appearing in the governing equations must be continuous (compatibility requirement).
2. All the field variables and all their derivatives of order not higher than the highest order of derivative appearing in the governing equations can be approximated as closely as required and in particular can take up any constant value when the size of any element tends to zero (completeness requirement).

Although the safest approach is to choose functions and formulate elements that satisfy these requirements we must mention that completeness alone is sufficient to prove convergence of the finite element methods, i.e., compatibility may be violated without resulting in divergent solutions [17]. As a matter of fact this was also found to be true in our method. Indeed, in the early development of the method we used a complete second order polynomial to represent a field component within a 2-D element with six nodes [18],

$$P_i(x,y) = a_{i,0} + a_{i,1}x + a_{i,2}y + a_{i,3}xy + a_{i,4}x^2 + a_{i,5}y^2 \tag{3.18}$$

where the subscript i denotes the i^{th} element. The six coefficients $a_{i,j}$ ($j = 0, 1, 2, \dots, 5$) were obtained from the six equations,

$$F_i(x_k, y_k) = P_i(x_k, y_k) \quad k = 1, 2, \dots, 6 \quad (3.19)$$

where F_i was any one of the field components at the six nodes (x_k, y_k) of the i^{th} element. It is obvious that the above interpolation function satisfies the completeness requirement but violates the compatibility one. Nevertheless this method showed convergence and very satisfactory results were produced.

We proceed next to a discussion of the two dimensional elements we are going to use and the interpolation functions associated with them.

A very attractive element is the four node quadrilateral. There exists two possible interpolation schemes for this element. The first one is the isoparametric quadrilateral developed by Ergatoudis et al. [19]. This is the one we are going to examine in detail. The second one uses rational functions for the interpolation over the element. A detailed discussion of this type of element can be found in [20].

Isoparametric Quadrilateral Elements

Natural Coordinates. Consider the quadrilateral of Fig. 3.6 and the coordinates η - ξ to be associated with it. These coordinates are in general curvilinear and will be so determined as to give

$$\eta = -1 \text{ on side (12)}$$

$$\eta = +1 \text{ on side (34)}$$

$$\xi = +1 \text{ on side (23)}$$

$$\xi = -1 \text{ on side (41)}$$

Assume that the relationship between the Cartesian coordinates x, y and the new coordinates η and ξ can be written in a general form

$$\mathbf{x} = \Phi_1 x_1 + \Phi_2 x_2 + \Phi_3 x_3 + \Phi_4 x_4 = \{\Phi\}^T \{X\} \quad (3.20)$$

$$\mathbf{y} = \Phi_1 y_1 + \Phi_2 y_2 + \Phi_3 y_3 + \Phi_4 y_4 = \{\Phi\}^T \{Y\}$$

where

$$\{X\} = \begin{Bmatrix} x_1 \\ x_2 \\ x_3 \\ x_4 \end{Bmatrix}; \quad \{Y\} = \begin{Bmatrix} y_1 \\ y_2 \\ y_3 \\ y_4 \end{Bmatrix},$$

and $\{\Phi\}^T = \{\Phi_1, \Phi_2, \Phi_3, \Phi_4\}$ are some functions of η and ξ . Once $\{\Phi\}$ is specified, given the nodal coordinates $\{X\}$ and $\{Y\}$ one can find the map (x, y) for any point (η, ξ) . Moreover, the sides of each element are defined as both x and y coordinates are given parametrically in terms of ξ or η . We realize that (3.20) define a mapping from $(\xi-\eta)$ to $(x-y)$ as shown in Fig. 3.7.

It is important to notice that since adjacent elements have to fit each other, their sides have to be uniquely determined by the common points. Hence, along the sides of the quadrilateral the coordinates x and y will be defined parametrically in terms of either ξ or η as linear functions. In order to specify $\{\Phi\}$ first notice that from (3.20) one requires:

$$\Phi_i = 1 \text{ at node } i \quad i = 1, 2, 3, 4$$

and

$$\Phi_i = 0 \text{ at node } j \neq i.$$

Then one can write by inspection:

$$\Phi_1 = \frac{1}{4}(1-\xi)(1-\eta)$$

$$\Phi_2 = \frac{1}{4}(1+\xi)(1-\eta)$$

$$\Phi_3 = \frac{1}{4}(1+\xi)(1+\eta)$$

$$\Phi_4 = \frac{1}{4}(1-\xi)(1+\eta)$$

or generally

$$\Phi_i = \frac{1}{4}(1 + \xi\xi_i)(1 + \eta\eta_i) \quad (3.21)$$

where ξ_i and η_i take their nodal values.

Once the functions Φ_i are found one has to define the variation of the field components over the element in terms of their nodal values. The isoparametric elements use as interpolation functions exactly the same functions Φ_i . Therefore in terms of the natural coordinates ξ and η one writes:

$$F^i(\xi, \eta) = \{\Phi\}^T \{F_m^i\}, \quad m = 1, 2, 3, 4 \quad (3.22)$$

where F^i is the i^{th} component of one of the fields and $\{F_m^i\}$ represents the nodal values of this component.

Since by construction the Φ 's have a linear variation along the sides of the element, the continuity of the field components is ensured and hence the compatibility requirement is satisfied. One can easily show that the completeness requirement is also satisfied [19].

Once the interpolation functions have been constructed, their partial derivatives with respect to x and y must be computed. Since the mapping (3.20) with Φ_i 's given by (3.21) is non-linear its inversion is not possible, therefore we have to work in terms of the natural coordinates ξ and η . Differentiating $\Phi_i(\xi, \eta)$ with respect to ξ and η we get

$$\begin{bmatrix} \frac{\partial \Phi_i}{\partial \xi} \\ \frac{\partial \Phi_i}{\partial \eta} \end{bmatrix} = \begin{bmatrix} \frac{\partial x}{\partial \xi} & \frac{\partial y}{\partial \xi} \\ \frac{\partial x}{\partial \eta} & \frac{\partial y}{\partial \eta} \end{bmatrix} \begin{bmatrix} \frac{\partial \Phi_i}{\partial x} \\ \frac{\partial \Phi_i}{\partial y} \end{bmatrix} = [\mathbf{J}] \begin{bmatrix} \frac{\partial \Phi_i}{\partial x} \\ \frac{\partial \Phi_i}{\partial y} \end{bmatrix} \quad (3.23)$$

where $[\mathbf{J}]$ is the Jacobian of the transformation. Solving for $\frac{\partial \Phi_i}{\partial x}$ and $\frac{\partial \Phi_i}{\partial y}$:

$$\begin{bmatrix} \frac{\partial \Phi_i}{\partial x} \\ \frac{\partial \Phi_i}{\partial y} \end{bmatrix} = [\mathbf{J}]^{-1} \begin{bmatrix} \frac{\partial \Phi_i}{\partial \xi} \\ \frac{\partial \Phi_i}{\partial \eta} \end{bmatrix} \quad (3.24)$$

Next, the derivatives $\partial F^i / \partial x$, $\partial F^i / \partial y$ are easily computed from (3.22)

$$\frac{\partial F^i}{\partial x} = \sum_{j=1}^4 \frac{\partial \Phi_j}{\partial x} F_j^i \quad (3.25a)$$

$$\frac{\partial F^i}{\partial y} = \sum_{j=1}^4 \frac{\partial \Phi_j}{\partial y} F_j^i \quad (3.25b)$$

Later in this section we shall see that an automatic mesh generation with quadrilaterals is easily implemented. One drawback of the isoparametric elements is the degeneration when one of the internal angles approaches π as depicted in Fig. 3.8. For $\alpha \geq \pi$, the inverse of the Jacobian $[\mathbf{J}]$ no longer exists and the mapping becomes non-unique. Therefore, one has to ensure that none of the elements is distorted close to degeneration in the mesh generation process.

Mesh generation

Our next step is to present the different ways of generating the finite element mesh. An extensive presentation of various techniques for the mesh generation can be found in [21]. Here, we only intend to present two easy to apply grid generation techniques.

(a) Mapping .

Consider the two dimensional geometry shown in Fig. 3.9a. The cross section of the conducting body is described mathematically by a single-valued function

$$r = f_s(\vartheta) \quad (3.26)$$

and the artificial boundary where the mesh terminates, by the single-valued

function:

$$r = f_b(\vartheta) \quad (3.27)$$

where (r, ϑ) are the polar coordinates of a point on the $x-y$ plane. Consider now the transformation:

$$\begin{cases} z = \frac{r - f_s(\vartheta)}{f_b(\vartheta) - f_s(\vartheta)} \\ \varphi = \vartheta \end{cases} \quad \vartheta \in [0, 2\pi] \quad (3.28)$$

It is apparent that under the above transformation the body contour Γ_1 and the boundary Γ_2 are mapped to the constant lines $z = 0$ and $z = 1$ respectively. The line $\vartheta = 0$ is transformed to the right and left sides of the transformed plane. Now, the generation of the mesh becomes obvious. First, a rectangular mesh is created on the transformed plane for the electric and magnetic nodes. Then, the inverse transformation

$$\begin{cases} r = f_s(\varphi) + z(f_b(\varphi) - f_s(\varphi)) \\ \vartheta = \varphi \end{cases} \quad (3.29)$$

is used for an automatic generation of the electric and magnetic mesh on the physical plane.

(b) Averaging

Consider the geometry shown in Fig. 3.10a and the rectangular grid shown in Fig. 3.10b. Readjust the points on the rectangle S_1 so that it deforms into the body contour Γ_1 . Then the point Q_1 has as coordinates those of the point Q'_1 . We do the same with the rectangle S_2 so that it deforms into the boundary Γ_2 . Because this rearrangement of the boundary points destroys the topology of the grid, an averaging procedure over the coordinates of the nodes of the grid is applied. The averaging procedure allows them to rearrange themselves in relation to those nodes which have been displaced on the contours Γ_1 and Γ_2 . For

example, for the point P of the rectangular mesh (see Fig. 3.10b) we have:

$$x_P = \frac{1}{4}(x_{Q3} + x_{P1} + x_{P2} + x_{P3}) \quad (3.30a)$$

$$y_P = \frac{1}{4}(y_{Q3} + y_{P1} + y_{P2} + y_{P3}) \quad (3.30b)$$

This averaging procedure is applied repeatedly until elements with satisfactory similarity in size result. Once the grid for the electric field has been constructed, the formation of a grid for the magnetic field is straightforward. For example, one can choose the magnetic nodes to be positioned at the centers of gravity of the resulting quadrilaterals.

The simplicity of the method is obvious. Sometimes, though, concave quadrilaterals might appear after the mesh generation. To avoid them, one sometimes has to specify the maps of additional points of the rectangular grid before the averaging procedure is applied.

The mesh shown in Fig. (3.3) has been generated using this method. The extension of the method to three dimensions is straightforward. A rigorous mathematical formulation of the method can be found in [21].

3.3. The Method of Conforming Boundary Elements

One of the great advantage of the finite difference method is the regularity of the nodal coordinates, since the index numbers of each node contain the nodal coordinates. The conforming element grid requires the storage of coordinates of all the nodes, which is very demanding on memory, especially for three-dimensional problems. The method of conforming boundary elements to be presented relaxes the large memory requirement by limiting the irregularly shaped elements to the boundary of the scatterer only. In addition to reducing the memory need, the method also has control of the size of the smallest element, while the other conforming methods leave that to chances, which for

stability reasons may sometimes limit the time increment to unrealistically small values.

Let us consider once again the conducting cylinder problem of 3.1. The cylinder is positioned on a rectangular mesh as shown in Fig. 3.11. The points of intersection of the cylindrical contour with the mesh will be nodes of null electric field if the mesh is chosen to be that of the electric nodes. Then it is obvious that one can use these nodes on the body contour together with some of the neighboring electric nodes on the regular mesh to form the boundary elements for the computation of the magnetic field. For example, the element (abE_3E_1) can be used for the computation of the magnetic field at node H_1 , the element (bcE_5E_3) for the node H_2 , the element $(klE_{23}E_{24})$ for the node of H_{14} etc. It is apparent that the boundary element method uses the uniform rectangular mesh everywhere in the computational domain except at the vicinity of the body contour. There, only a few variety of quadrilateral elements are needed for us to conform to the scatterer geometry. Since it is only necessary to store the coordinates of the boundary element nodes, the storage requirement is substantially reduced.

There are some restrictions regarding the size of the boundary element. For reasons of stability, the elements as those in Fig. 3.12 must be avoided. Our experience is that dealing with smooth geometries, the most frequently encountered boundary elements that can be used without affecting the stability of the numerical solution are the ones shown in Fig. 3.13. It should also be noticed that there are some electric and magnetic nodes in the vicinity of the body contour which need special treatment. Consider for example the element $(fhE_{13}E_9)$ in Fig. 3.11. This element is used for the computation of the magnetic field at the node H_7 . Notice though that there is no appropriate boundary element for the computation of the magnetic field at node H_6 . Since the mag-

netic field at this node is needed for the future computation of the electric field at node E_{12} we have to use some other way to compute it. A simple way is to extrapolate the value from the neighboring magnetic nodes. In the same element we notice that the electric nodes E_8 and E_{11} are not enclosed by a magnetic element, therefore again one uses interpolation to compute their values from the values of the neighboring electric nodes.

The last thing about the boundary element method and its application for 2-D problems is some modifications that must be done when the incident plane wave pulse has the magnetic field vector parallel to the axis of the cylinder.

The Maxwell's equations are now:

$$\frac{\partial H_z}{\partial t} = -\frac{1}{\mu} \left(\frac{\partial E_y}{\partial x} - \frac{\partial E_x}{\partial y} \right) \quad (3.31a)$$

$$\frac{\partial E_x}{\partial t} = \frac{1}{\epsilon} \frac{\partial H_z}{\partial y} \quad (3.31b)$$

$$\frac{\partial E_y}{\partial t} = -\frac{1}{\epsilon} \frac{\partial H_z}{\partial x} \quad (3.31c)$$

On the conducting surface we know that the tangential component of the electric field is zero. Therefore,

$$\hat{n} \times \bar{E}^{sc} = -\hat{n} \times \bar{E}^{in} \quad (3.32)$$

But, the electric field has both normal and tangential components and (3.32) alone is not enough for the specification of the scattered electric field on the body surface. The boundary condition of (3.32) may be supplemented with the continuity equation on the body surface:

$$\nabla \cdot \bar{J} + \frac{\partial \rho}{\partial t} = 0 \quad (3.33)$$

where

$$\bar{\mathbf{J}} = \hat{\mathbf{n}} \times \bar{\mathbf{H}}^{total} \quad (3.34a)$$

$$\rho = \hat{\mathbf{n}} \cdot \bar{\mathbf{D}}^{total} \quad (3.34b)$$

Substituting $\bar{\mathbf{J}}$ and ρ in (3.33), we get

$$\nabla_0 \cdot (\hat{\mathbf{n}} \times \bar{\mathbf{H}}^t) = -\epsilon \hat{\mathbf{n}} \cdot \frac{\partial \bar{\mathbf{E}}^{total}}{\partial t} \quad (3.35)$$

where ∇_0 is the surface divergence, requiring derivatives along the surface of the body only. (3.32) and (3.35) constitute a system of equations for the computation of the two components of the electric field on the scatterer. Once the scattered electric field is known on the body surface one can compute the magnetic and electric field everywhere on the mesh following the same procedure as in 3.1.

Let us see now how equations (3.32) and (3.35) can be used in the irregular boundary elements. Consider the geometry of Fig. 3.14. We want to update the electric field at point E . Let $\hat{\mathbf{n}}$ and $\hat{\boldsymbol{\tau}}$ be the unity normal and tangential vectors at E , respectively,

$$\hat{\mathbf{n}} = n_x \hat{\mathbf{x}} + n_y \hat{\mathbf{y}} \quad (3.36a)$$

$$\hat{\boldsymbol{\tau}} = -n_y \hat{\mathbf{x}} + n_x \hat{\mathbf{y}} \quad (3.36b)$$

Since the surface divergence requires derivatives along the surface only, one finds that

$$\nabla_0 \cdot (\hat{\mathbf{n}} \times \bar{\mathbf{H}}^{total}) = n_y \frac{\partial H^{total}}{\partial x} - n_x \frac{\partial H^{total}}{\partial y} \quad (3.37)$$

and hence, equation (3.35) gives,

$$n_y \frac{\partial H^{total}}{\partial x} - n_x \frac{\partial H^{total}}{\partial y} = -\epsilon \left[n_x \frac{\partial E_x^{total}}{\partial t} + n_y \frac{\partial E_y^{total}}{\partial t} \right] \quad (3.38)$$

On the other hand, equation (3.32) becomes,

$$n_x E_y^{sc} - n_y E_x^{sc} = n_y E_x^{in} - n_x E_y^{in} \quad (3.39)$$

It is now apparent that eqs. (3.38) and (3.39) constitute a system for the computation of $E_x^{sc}(t_0 + \Delta t)$, $E_y^{sc}(t_0 + \Delta t)$ from their previous values $E_x^{sc}(t_0)$, $E_y^{sc}(t_0)$, the knowledge of the incident field at that point and the spatial derivatives of the magnetic field computed at $t = t_0 + \frac{1}{2}\Delta t$.

In order to compute these spatial derivatives of the scattered magnetic field in the boundary element method we introduce the nodes S_1, S_2, S_3, \dots which are the points of intersection of the scatterer with the magnetic mesh. Their values can be computed using extrapolation. For example the magnetic field at S_2 and S_1 can be found by extrapolating its values at H_2 and H_1 respectively. Then, it is a simple matter to find the spatial derivatives $\partial H / \partial x$, $\partial H / \partial y$ at E , using the interpolation function over the element $(S_1 H_1 H_2 S_2)$.

Let us now summarize the key points in the boundary element method. Arbitrarily deformed quadrilaterals are used merely in the vicinity of the body surface and it is only for these quadrilaterals that one has to store the coordinates of their nodes. One also has to store those magnetic nodes which are computed by extrapolation and those electric nodes where interpolation must be used in order to update their values. Finally, if one solves the case with the magnetic field parallel to the z -axis the normal derivatives on the surface of the body at the points where the contour intersects the electric mesh must be known, as well as the points where the magnetic mesh intersects the body contour.

3.4. Numerical Considerations

(i) Stability and Convergence

Discrete approximations to partial differential equations are useful only if they are convergent and stable. It is well known that the problem of

convergence consists of finding the conditions under which the difference between the theoretical solutions of the differential and the discretized equations at a fixed point (\bar{x}, t) , tend to zero uniformly, as the net is refined in such a way that $h, \Delta t \rightarrow 0$ and $m_i, n \rightarrow \infty$, ($i=1,2,3$), with $m_i h (=x_i)$ and $n \Delta t (=t)$ remaining fixed. On the other hand, the problem of stability consists of finding a condition under which the difference between the theoretical and numerical solutions of the discretized equation, remains bounded as n tends to infinity. Lax and Richtmyer have shown [22] that if a linear difference equation is consistent with a properly posed linear initial-value problem, then stability is the necessary and sufficient condition for convergence. The hyperbolic system

$$-\mu \frac{\partial \bar{H}}{\partial t} = \nabla \times \bar{E} \quad (3.40a)$$

$$\varepsilon \frac{\partial \bar{E}}{\partial t} = \nabla \times \bar{H} \quad (3.40b)$$

for $t \in [0, \infty)$ with initial conditions

$$\bar{E}(\bar{r}, 0) = \bar{F}_1(\bar{r}); \quad \bar{H}(\bar{r}, 0) = \bar{F}_2(\bar{r}) \quad (3.41)$$

on a domain without boundaries is a properly posed initial-value problem called Cauchy problem. Since the leap-frog scheme introduced in Section 3.1 is a consistent difference approximation to the above Cauchy problem, we only need to examine the condition under which stability is ensured. There are several ways of analyzing the stability of a hyperbolic system on a regular square grid [23]. Wilson [24] has shown that the leap-frog scheme is stable if

$$c(\Delta t) \leq h \quad (3.42)$$

where c is the velocity of propagation. It is interesting to notice that this stability criterion is independent of the number of dimensions if the computational grid is uniform, that is, the mesh increment h is the same along any dimension. This is an advantage over the *TDFD* scheme where the stability condition

depends on the number of dimensions n as

$$c(\Delta t) \leq \frac{h}{\sqrt{n}} \tag{3.43}$$

It is not an easy task to derive a stability criterion for a grid with irregular elements. Nevertheless one can use the theory by Courant, Friedrichs and Lewy [25] to show that (3.42) can be used as the stability condition for the leap-frog scheme on a partially irregular grid as long as each of its irregular elements is large enough to contain a regular element of the grid. (See Fig. 3.13)

An added complication is the presence of the absorbing boundary, which necessitates a selection of additional numerical boundary conditions which are not present in the original problem. Unless great care is taken, these boundary conditions can lead to instabilities in the numerical calculation. For the case of hyperbolic systems, the stability question is solved in principle by the theory of Gustafsson, Kreiss and Sundström [26]. Application of this theory, however, is difficult because of its complexity and abstractness. Nevertheless, a simple physical interpretation of the main result of this theory was given recently in terms of group velocity [27]. It is well known that group velocity is a concept associated with energy propagation under dispersive conditions. Its significance to numerical stability results from the fact that finite difference models, even of nondispersive equations, are necessarily dispersive. As an example, consider the problem

$$\frac{\partial u}{\partial x} - \frac{1}{c} \frac{\partial u}{\partial t} = 0 \tag{3.44}$$

for $x \in (-\infty, \infty)$, $t \in [0, \infty)$ and the initial condition

$$u(x, 0) = f(x) \tag{3.45}$$

The solution of course is a leftward translation of speed c , that is, $u(x, t) = f(x + ct)$. In the frequency domain one looks for wave solutions of the

form:

$$u(x, t) = e^{-j(\omega t - \xi x)} \quad (3.46)$$

where ξ is the wavenumber. Then from (3.4.5) one has

$$\omega = -c \xi \quad (3.47)$$

which is the dispersion relation for (3.44). Let us now approximate (3.44) with the finite difference equation

$$U_i^{n+1} = U_i^{n-1} + c \frac{\Delta t}{h} (U_{i+1}^n - U_{i-1}^n) \quad (3.48)$$

on a uniform grid with space step h , where

$$U_i^n \approx u(ih, n\Delta t), \quad -\infty < i < \infty, n \geq 0$$

Substitution of (3.46) into (3.48) gives

$$\sin \omega \Delta t = -c \frac{\Delta t}{h} \sin \xi h \quad (3.49)$$

We know that energy associated with wave number ξ will propagate at a group velocity given by

$$c_g = \frac{d\omega}{d\xi} \quad (3.50)$$

Then (3.47) gives the group velocity $c_g = -c$ for equation (3.44), while (3.49) gives the group velocity

$$c_g = -c \frac{\cos(\xi h)}{\cos(\omega \Delta t)} \quad (3.51)$$

We see that the difference approximation (3.48) is **dispersive**, that is, energy associated with different wavenumbers or frequencies will travel at different group velocities, although the starting equation (3.44) is **non-dispersive**.

Based on this, one can state the main result in the theory of Gustafsson, Kreiss and Sundström as following [27]. An initial boundary value problem

model is stable if and only if

- (i) the stability condition of (3.42) is satisfied everywhere inside the mesh boundary.
- (ii) the model (including boundary conditions) admits no plane wave solutions that grow from each time step to the next by a constant factor z with $|z| > 1$ and
- (iii) the model (including boundary conditions) admits no wave solutions with group velocities which support active radiation from the artificial boundary to the interior of the domain of computation.

An absorbing boundary condition model based on this theory is presented in Section 5.

(ii) Exciting pulse and space sampling.

The usefulness of computing in time domain is that in principle a **single** computation with an arbitrary exciting pulse can provide the response characteristics of the target for all frequencies. In practice though, one has to deal with the "noise" introduced by the numerical processing which affects the high frequency information. This effect could be minimized if the exciting pulse had the widest possible bandwidth. Such a pulse would approach the delta function and numerically one does it by using a Gaussian pulse $g(t)$ given by (see Fig. 3.15).

$$g(t) = e^{-t^2/T^2} \tag{3.52}$$

whose spectrum $G(f)$ is

$$G(f) = e^{-\pi^2 f^2 T^2} \tag{3.53}$$

Notice that at $f = 1/2T$, $G(f) \approx 0.1$ and if we define the effective bandwidth on this basis, we conclude that the duration of the pulse determines its effective

maximum frequency, $f_{\max} = 1/2T$.

On the other hand, we saw that because of the dispersive characteristics of the finite difference approximation, an initial signal that is not monochromatic will change form as it propagates. Following the procedure in (i) one can show that the dispersion relation for Maxwell's equations in one dimensional space is:

$$\sin^2 \frac{\omega \Delta t}{2} = \left(c \frac{\Delta t}{h}\right)^2 \sin^2 \frac{\xi h}{2} \quad (3.54)$$

For a well resolved wave one has $\xi h \approx 0$ and $\omega \Delta t \approx 0$ and from (3.54)

$$\left(\frac{\omega \Delta t}{2}\right)^2 \approx \left(c \frac{\Delta t}{h}\right)^2 \left(\frac{\xi h}{2}\right)^2$$

That is, if we can keep $\omega \Delta t$ small enough, the dispersive effects of the finite difference approximation are minimized.

A sufficient choice would be

$$\frac{\omega \Delta t}{2} < \frac{\pi}{12} \Rightarrow 2\pi \frac{c}{\lambda} \Delta t < \frac{\pi}{6} \Rightarrow c \Delta t < \frac{\lambda}{12}$$

Hence, for the minimum wavelength in the spectrum of the exciting pulse the relation

$$\lambda_{\min} > 12(c \Delta t)$$

must hold. Or, because of the stability limit $c \Delta t < h$ one can consider the relation

$$\lambda_{\min} > 12h \quad (3.56)$$

as a sufficient condition for minimizing the dispersive effects. Since for the Gaussian pulse (3.52) the effective minimum wavelength is $\lambda_{\min} = 2cT$, it is apparent that if one chooses T such that

$$2cT > 12h \quad (3.57)$$

the pulse will propagate down the grid without significant distortion. Numerical

experimentation showed that for a one-dimensional grid, the condition in (3.57) was too conservative. Actually, a Gaussian pulse as short as $5h$ was found to propagate down the grid without distortion. As the dimensions of the problem increase though, another type of error occurs in the numerical approximation of hyperbolic equations. That is, the velocity of propagation of numerical sinusoidal solutions in addition to being dependent upon frequency, is also dependent upon direction of propagation. This numerical anisotropy depends on the space discretization [28]. A polar diagram of the normalized phase velocity c^*/c as a function of wavelength λ and direction of propagation α for the discretization scheme (3.17), is shown in Fig. 3.16. It is apparent that for wavelengths longer than $8h$, the anisotropy is almost negligible. Hence, for two dimensional problems, the condition in (3.57) can be relaxed to the following one,

$$2cT > 8h \quad (3.59)$$

We must also mention that (3.59) must be applied for the lowest velocity c in the domain of computation. The exciting pulse should also start and end smoothly enough to avoid spurious oscillations. These oscillations are familiar in finite-difference computations; see [28] for illustrations.

Finally, the ratio of body size to the effective spatial width of the pulse is also important. We know that the scattering characteristics of a structure can be described in terms of its poles in the complex frequency domain. The number of these poles is determined by the effective maximum frequency, f_{\max} , of the exciting pulse, which, as we discussed earlier, is determined by the spatial width of the pulse. On the other hand, the locations of the poles in the complex plane scale directly with the size of the body. Hence, for accurate information on the nature of the target, one should increase f_{\max} , that is, decrease the pulse width. This, then, results in using smaller width for the

spatial and temporal samples, which of course increases the storage requirements and the computational time. That is, there is a tradeoff between accurate high-frequency information and cost of computation.

3.5. Dielectric Interfaces

At the interface between two media with different dielectric constants, the field components or their derivatives are discontinuous. Therefore the interpolation functions over elements that include the interface must be modified to include the appropriate discontinuity. Because the construction of such an interpolation function is rather complicated, an easier technique will be presented here.

Consider the following set of Maxwell's equations,

$$\frac{\partial H_z}{\partial t} = -\frac{1}{\mu_0} \left(\frac{\partial E_y}{\partial x} - \frac{\partial E_x}{\partial y} \right) \quad (3.60a)$$

$$\frac{\partial E_x}{\partial t} = \frac{1}{\epsilon} \frac{\partial H_z}{\partial y} \quad (3.60b)$$

$$\frac{\partial E_y}{\partial t} = -\frac{1}{\epsilon} \frac{\partial H_z}{\partial x} \quad (3.60c)$$

Figure 3.17 shows an electric element which includes the dielectric interface. Equations (3.60a) must be used in order to update the magnetic field at the H node. The dielectric interface is approximated by a straight line. Consider the coordinate system (ξ, η) centered at H with axes ξ and η parallel and normal to the dielectric interface, respectively. In this coordinate system, equation (3.60a) is written:

$$\frac{\partial H_z}{\partial t} = -\frac{1}{\mu_0} \left(\frac{\partial E_\eta}{\partial \xi} - \frac{\partial E_\xi}{\partial \eta} \right) \quad (3.61)$$

Notice now that the derivative $\frac{\partial E_\eta}{\partial \xi}$ can be approximated as

$$\frac{\partial E_\eta}{\partial \xi} \cong \frac{E_n(C) - E_n(A)}{2d} \quad (3.62)$$

where C and A are the points of intersection of the ξ axis with the upper and lower sides of the element. Of course, the electric field at these points must be found by extrapolation from the neighboring nodes on the same side since discontinuity of the electric field along the interface does not allow interpolation.

On the other hand E_ξ is continuous along the interface and also its derivative is continuous permitting us to write:

$$\frac{\partial E_\xi}{\partial \eta} \cong \frac{E_\xi(D) - E_\xi(A)}{2d} \quad (3.63)$$

Using (3.63) and (3.62) in (3.61) the magnetic field at H is then updated.

Consider now the other two equations (3.60b) and (3.60c) which must be solved over the magnetic element shown in Figure 3.18 in order to update the electric field at the E -node. In the coordinate system (ξ, η) these equations becomes:

$$\frac{\partial E_\xi}{\partial t} = \frac{1}{\epsilon} \frac{\partial H_z}{\partial \eta} \quad (3.64a)$$

$$\frac{\partial E_\eta}{\partial t} = -\frac{1}{\epsilon} \frac{\partial H_z}{\partial \xi} \quad (3.64b)$$

Notice then that E_η is easily updated by approximating the derivative $\partial H_z / \partial \xi$ by

$$\frac{\partial H_z}{\partial \xi} \cong \frac{H_z(C) - H_z(A)}{2d} \quad (3.65)$$

Since both points A and C belong in the same medium, no discontinuities are involved in this computation. Of course, if the electric node coincides with the dielectric interface, it becomes a double-valued node and one must be careful to

keep that in mind when updating the magnetic field on either side of the interface the next time step.

Finally we have to deal with equation (3.64a). Notice that although H_z is continuous along the interface, its derivative along the direction normal to the interface has a discontinuity such that the product $\frac{1}{\epsilon} \frac{\partial H_z}{\partial \eta}$ is a continuous function along η . The variation of H_z with η is shown in Fig. 3.19a.

If for a moment we assume that dielectric material ϵ_1 was covering the whole space, then the values of H_z at points D and B would be $H_z(D)$ and $H_z^f(B)$, where the index f is being used to distinguish the fictitious value from the true value $H_z(B)$. Then we would write:

$$\frac{\partial E_{\xi}}{\partial t} \cong \frac{1}{\epsilon_1} \frac{H_z(D) - H_z^f(B)}{2d} \quad (3.66a)$$

and the value of the magnetic field at the interface would be:

$$H_z(I) = H_z(D) + (H_z^f(B) - H_z(D)) \left(\frac{d - \eta_0}{2d} \right) \quad (3.66b)$$

(see Fig. 3.19b). Using the same reasoning, but assuming now that the whole space is covered with dielectric material ϵ_2 , the value of H_z at D will now be the fictitious one and we could write:

$$\frac{\partial E_{\xi}}{\partial t} \cong \frac{1}{\epsilon_2} \frac{H_z^f(D) - H_z(B)}{2d} \quad (3.67a)$$

and

$$H_z(I) = H_z^f(D) + (H_z(B) - H_z^f(D)) \left(\frac{d - \eta_0}{2d} \right) \quad (3.67b)$$

(See Fig. 3.19c.) Since E_{ξ} and H_z are continuous at the interface, the right hand sides of equations (3.66a), (3.67a) and (3.66b), (3.67b) are equal and hence we can write:

$$H_z(D) + (H_z^f(B) - H_z(D)) \left[\frac{d - \eta_0}{2d} \right] = H_z^f(D) + (H_z(B) - H_z^f(D)) \left[\frac{d - \eta_0}{2d} \right] \quad (3.68a)$$

$$\frac{1}{\epsilon_1} (H_z(D) - H_z^f(B)) = \frac{1}{\epsilon_2} (H_z^f(D) - H_z(B)) \quad (3.68b)$$

From the above equations one can solve for one of the fictitious points $H_z^f(B)$ or $H_z^f(D)$, the choice depending on the position of the electric node and then substitute in (3.66a) or (3.67a) respectively in order to get a semi-discrete expression for the time derivative of E_ξ . For example, for the case of Fig. 3.18, solving for $H_z^f(B)$ we find:

$$H_z^f(B) = H_z(D) \frac{\left[1 - \frac{\epsilon_1}{\epsilon_2} \right]}{\left[1 + K \frac{\epsilon_1}{\epsilon_2} \right]} + H_z(B) \frac{\left[\frac{\epsilon_1}{\epsilon_2} \right] (1 + K)}{\left[1 + K \frac{\epsilon_1}{\epsilon_2} \right]} \quad (3.69)$$

where

$$K = \frac{1 - \frac{\eta_0}{d}}{1 + \frac{\eta_0}{d}} \quad (3.70)$$

Of course, the values $H_z(B)$ and $H_z(D)$ are found by interpolation on the two sides of the magnetic element.

Although the above technique was presented for the case of an electromagnetic field with the magnetic field polarized along z , its modification for the case of the electromagnetic wave with the electric field polarized along z is straightforward.

To summarize, the above technique provides a simple computational procedure for treating dielectric interfaces. The only additional information needed is the inclination φ of the line approximating the interface inside the

boundary element with respect to the x -axis, as well as the x coordinate x_0 , of the point where this line intersects the x -axis of the local coordinate system centered at the center of gravity of the element. (See Fig. 3.18).

3.6. Numerical Example.

As with all finite-element methods, an important part of the numerical computation is related to the generation of the computational mesh with its special boundary elements and the rest of the necessary information regarding the characteristics of the geometry of the scatterer. For this purpose, a very general code has been written for the mesh generation in two dimensions. This code can handle arbitrary cross sections and is written in such a way that with a few modifications, it can treat more general problems like many bodies scattering, electromagnetic coupling, etc. Once the information regarding the specific geometry has been generated, the second part of the computer program solves the discretized time dependent Maxwell's equations for the evaluation of the electric and magnetic fields everywhere on the computational mesh.

Due to restrictions of space and since results for the scattering by conducting cylinders using this technique have already been presented in [18], we chose as the numerical example the focussing effect of a cylindrical type Maxwell's fish-eye lens, Fig. 3.20. The relative dielectric permittivity of the lens,

$$\epsilon_R = \frac{4}{[1 + (r/a)^2]^2}$$

varies nonlinearly with radius from four at the origin to one at $r = a$. According to ray theory, a line source at the focus would result in plane waves emerging from the plane surface of the lens [39].

In the sequence of Fig. 3.21 we see how a plane wave is focussed upon entering the lens. The incident pulse was the Gaussian pulse of Fig. 3.15 with the parameter T chosen so that the width of the pulse is about the radius of the

lens. The little arrows represent the Poynting vector at each point showing the intensity of the wave and visualizing its propagation.

4. Extension to Three-Dimensions

The discussions of the previous sections are for computations in one and two dimensions. Basically, the theories and techniques can all be extended to three-dimensional problems, although the effort to implement the method will increase drastically due to the additional dimension. For example, the program that produces the results in Section 3 is well automated so that only scatterer geometry is required for the input and the boundary elements are constructed without any further instruction from the user. To program such user friendly input will involve much more effort because of the additional dimension. Computations of three dimensional problems in time domain have been attempted by Kunz and Lee [3] and Taflove and Brodwin [4], but their programs are not automated, even though their mesh configurations are simple grids without conforming elements.

Bodies of revolution is a class of three dimensional scatterers, which can be solved with much less memory. By expanding the incident waves into azimuthal modes, one can solve each mode separately as a two dimensional problem. Since the motivation of the time domain finite element method is to make use of the tremendous memory capacities available in a supercomputer to solve arbitrary three dimensional problems, we shall not discuss the particulars regarding bodies of revolutions even though such are problems readily solvable directly with the techniques discussed earlier.

The conforming boundary elements used in three dimensions are hexahedrons, such as shown in Fig. 4.1. Isoparametric elements can still be used in this case, where the interpolation in natural coordinates is tri-linear,

$$U(\xi, \eta, \zeta) = \sum_{i=1}^8 L_i(\xi, \eta, \zeta) U_i \quad (4.1)$$

and the mapping is defined as

$$\mathbf{x} = \sum_{i=1}^8 L_i(\xi, \eta, \zeta) \cdot \mathbf{x}_i \quad (4.2a)$$

$$\mathbf{y} = \sum_{i=1}^8 L_i(\xi, \eta, \zeta) \cdot \mathbf{y}_i \quad (4.2b)$$

$$\mathbf{z} = \sum_{i=1}^8 L_i(\xi, \eta, \zeta) \cdot \mathbf{z}_i \quad (4.2c)$$

where

$$L_i = \frac{1}{8}(1 + \xi\xi_i)(1 + \eta\eta_i)(1 + \zeta\zeta_i), \quad i = 1, 2, \dots, 8 \quad (4.3)$$

It is noted that one of the surfaces of a conforming boundary element may not be a plane, nevertheless equations (4.2) can still provide us with a parametric representation of a second order surface that approximates the geometry of interest.

Although the basic idea on radiation conditions may also be extended to 3-D cases, care must be taken on the longitudinal components, which may not be negligibly small compared to the transverse component on surfaces close to the scatterer. Further discussion on this point will be included in Section 5. Another important issue in 3-D computation using a super computer is memory management, which can greatly effect the speed of the computation. A general program of 3-D time domain computation using point-matched finite element method is still in progress. We hope to discuss the details in a future treatise.

5. Radiation Boundary Condition

As we have discussed in Section 2.1, the uniqueness of Maxwell's equation requires the knowledge of the tangential components of \vec{E} or \vec{H} on the boundary

for all time $t \geq 0$. For a scattering problem, the boundary condition at infinity is known as Sommerfeld's radiation condition [29], where the fields are limited to those of outward travelling wave type. In the numerical simulation of a scattering problem, the radiation conditions are approximated at a finite surface which encloses the scatterer. The surface needs to be large enough for good approximation and close to the scatterer to reduce the numerical solution domain. Later we will see that a rule of thumb for relative dimensions between the scatterer and the radiation boundary can be given such that reasonable approximations are obtained.

Numerically, the radiation boundary condition may be considered as a necessary part of the algorithm to terminate the computation at a finite boundary. An example of such a treatment in a one-dimensional case has been presented in Sec. 2.1 where the field at the terminating boundary is computed from values inside the numerical solution domain using the condition of an outgoing wave. The differential equations cannot be used to compute the fields on the terminating boundary since it would require the field values outside of the latter. In two and three dimensional problems, the approximations of radiation conditions are more difficult, because the condition of outgoing wave requires the a priori knowledge of the direction of wave propagation. There is a large amount of literature devoted to this subject [30]-[36]. The most intuitive and computationally simple method is to use lossy material layers surrounding the radiating source. Unfortunately, for effective suppression of reflections, the loss must be increased very gradually, i.e., the absorbing layer may extend beyond several wavelength of the lower spectrum frequency content of the pulse which results in wastefully large computation space. A simple extrapolation of the boundary fields from nodal values adjacent to the latter almost always results in instability [37]. An exact termination method using Huygen's principle [36] is guaranteed to work, but is expensive both in storage and computation, since

both the electric and magnetic fields are required on the surface adjacent to the boundary and the Green's dyads needs to be computed in the subsequent surface integrals.

An ideal terminating method is one which can effectively suppress reflections and also involves only local (in space and in time) operations consistent with the simple algorithm of the finite difference or finite-element method. Engquist and Majda [33] have introduced pseudo-differential operators, or equivalent parabolic approximations to the hyperbolic equation, to separate incoming and outgoing waves on the boundary. However, some stability problems occur when it is applied in cartesian coordinates. Bayliss and Turkel's boundary conditions [35] are based on the global field expansion for outgoing waves of Friedlander [38], which is a time domain equivalent of Sommerfeld's expansion in frequency domain [29]. Friedlander has shown that the expansion,

$$u(t, r, \vartheta, \varphi) = \sum_{i=1}^{\infty} \frac{f_i(t - \frac{r}{c}, \vartheta, \varphi)}{r^i} \quad (5.1)$$

is a solution of scalar wave equation if f_1 is a regular function of ϑ and φ on a spherical surface that encloses all the sources and f_i 's are unique for any outgoing wave from the latter. Bayliss and Turkel propose a family of differential operators, B_m , which annihilates the first m terms in (5.1),

$$B_1 = \frac{1}{c} \frac{\partial}{\partial t} + \frac{\partial}{\partial r} + \frac{1}{r} \quad (5.2)$$

$$B_m = \left(\frac{1}{c} \frac{\partial}{\partial t} + \frac{\partial}{\partial r} + \frac{2m-1}{r} \right) B_{m-1} \quad (5.3)$$

Application of the differential operators B_m is equivalent to enforcing the field continuity with first m terms of the expansion (Fig. 5.1). For many practical modelings, where the radiation field dominates near the boundary, B_1 is sufficient to suppress reflections. In such cases, the field near the radiation

boundary behaves like

$$u(t, r, \vartheta, \varphi) \cong \frac{f_1(t - \frac{r}{c}, \vartheta, \varphi)}{r} \quad (5.4)$$

Hence we can extrapolate the boundary value from the knowledge of the interior field by

$$u(t, r_b, \vartheta, \varphi) = \frac{r_0}{r_b} u(t - \frac{r_b - r_0}{c}, \vartheta, \varphi) \quad (5.5)$$

In the actual implementation of the method, it is convenient to choose the interior point r_0 such that the time retardation $\frac{r_b - r_0}{c}$ is equal to the time increment Δt (Fig. 5.2). Then the boundary value can be directly updated from the interior field value at the previous time step,

$$u(t_{n+1}, r_b, \vartheta, \varphi) = \frac{r_b - c \cdot \Delta t}{r_b} u(t_n, r_b - c \cdot \Delta t, \vartheta, \varphi) \quad (5.6)$$

In two-dimensional cases, the radial attenuation factor must be modified in (5.6) and we must use,

$$u(t_{n+1}, r_b, \varphi) = \sqrt{\frac{r_b - c \cdot \Delta t}{r_b}} u(t_n, r_b - c \cdot \Delta t, \varphi) \quad (5.7)$$

The above boundary conditions (5.6) and (5.7) satisfy the stability criteria of Gustafsson, Kreiss and Sundström [26] and in fact give rise to well-behaving solutions.

Bayliss and Turkel's boundary conditions for scalar wave equation apply directly to the components of solution of Maxwell's equations provided that they satisfy the corresponding scalar wave equation, i.e., those components behave like potentials. As a matter of fact in the two-dimensional case, the problem can be conveniently decomposed into transversal electric to z ($E_z \equiv 0$) and transversal magnetic to z ($H_z \equiv 0$), and the field extrapolation (5.7) can be applied to H_z

and E_z , respectively. Hence we will terminate the numerical solution domain with the magnetic field nodes (H_z) on the boundary in the former, and with the electric field nodes (E_z) in the latter case. In fact, our numerical example for Maxwell's lense in Section 3.6 was computed making use of (5.7) which was applied to E_z .

For arbitrary three-dimensional problems, it is well known that rE_r and rH_r behave like potentials in spherical coordinates [39]. Therefore we can apply (5.6) and obtain,

$$\begin{pmatrix} E_r \\ H_r \end{pmatrix}(t_{n+1}, r_b, \vartheta, \varphi) = \left[\frac{r_b - c \cdot \Delta t}{r_b} \right]^2 \begin{pmatrix} E_r \\ H_r \end{pmatrix}(t_n, r_b - c \cdot \Delta t, \vartheta, \varphi) \tag{5.8}$$

In principle, other components on the boundary must be computed from E_r and H_r . Unfortunately, the relationships expressing $E_\vartheta, E_\varphi, H_\vartheta$ and H_φ in terms of E_r and H_r are not simple, and hence not suitable for direct numerical implementation. However, it can be shown that for large r , the ϑ and φ components asymptotically admit solutions which behave like (5.4) and we can therefore make direct use of the field extrapolation (5.6).

The main advantage of Bayliss and Turkel's method rely on the fact that it is geometry independent, i.e., the field extrapolation (5.6) or (5.7) can be applied to any convenient form of radiation boundary provided that the coordinate point $(r_b - c \cdot \Delta t, \vartheta, \varphi)$ is located inside the computational domain D .

Up to this point, we have not yet specified two important pieces of information needed to successfully apply the above technique; namely the choice of an appropriate origin and the relative dimension of the computational domain with respect to the source or the scatterer. It is obvious that the performance of the method depends heavily on an apparently arbitrary choice of those two parameters. As a general rule, the following guidance must be observed;

- 823
- (i) The distance from the source or the scatterer to the radiation boundary must be large so that only the radiation field dominates in the neighborhood of the latter. Otherwise, higher order terms in expansion (5.1) become non-negligible.
 - (ii) The origin must be located near the center of the source or the scatterer. Sometimes, such a choice is not obvious and it is necessary to adjust the location in order to minimize the reflection.
 - (iii) For the equivalent point source at the origin to be able to approximately represent the actual outgoing waves, the minimum distance across the computational space must be at least twice the maximum dimension of the structure of interest (Fig. 5.3).

The main drawback of Bayliss and Turkel's 1st condition B_1 arises from the assumption that the radiation field propagates along the radial line from the origin. It is understandable that such an approximation is asymptotic in the radial distance and there is a limit in shrinking the size of the computational domain without sacrificing the solution accuracy. The underlying idea of an alternative method, namely the "Poynting Vector" method, is to predict the direction of field propagation from the interior fields using;

$$\bar{S} = \bar{E} \times \bar{H} \quad (5.9)$$

In general, the Poynting vector \bar{S} represents the flow of the energy density in every point of space and its direction coincides in an average sense with that of the propagation of the wave front. As a matter of fact, a distributed source often creates a wave front which moves in the direction of Poynting vector \bar{S} (Fig. 5.4). However this is not always true and the following example demonstrates an exception. Consider two line-sources each radiating independently. The total Poynting vector at point P is the sum of individual Poynting vectors and the interaction energy densities (Fig. 5.5),

$$\begin{aligned}\bar{S} &= (\bar{E}_1 + \bar{E}_2) \times (\bar{H}_1 + \bar{H}_2) = \bar{E}_1 \times \bar{H}_1 + \bar{E}_2 \times \bar{H}_2 + \bar{E}_2 \times \bar{H}_1 + \bar{E}_1 \times \bar{H}_2 \\ &= \bar{S}_1 + \bar{S}_2 + \bar{S}_{21} + \bar{S}_{12}\end{aligned}\quad (5.10)$$

If \bar{E}_1 and \bar{E}_2 have the same polarity, \bar{S} points somewhere in between the vector \bar{S}_1 and \bar{S}_2 , indicating the average direction of propagation. However if one changes \bar{E}_1 to $-\bar{E}_1$ and \bar{H}_1 to $-\bar{H}_1$, \bar{S}_1 remains the same, but the total vector \bar{S}' now points towards a wrong direction outside the region 1. Also in some cases $\bar{E}_1 = -\bar{E}_2$ at certain time and points, which result in $\bar{S} = 0$, making the extrapolation impossible. Hence the Poynting vector method finds its full potential in the solution which does not contain rapid inversion of the field such as multiple reflections between two conducting surfaces. It is particularly useful for modeling reflector antennas or dielectric lenses possessing strong focussing effects. However, there still remains the choice of an appropriate origin which, if not correctly set, will dramatically offset the advantage of the method.

So far, we were concerned with the radiation condition in non-dissipative medium. If the medium is lossy, the field extrapolation (5.6) or (5.7) must be modified accordingly; due to the dispersion effect of the loss, the correct field extrapolation requires a convolution integral. However, it can be shown that this dispersion effect is negligible for most practical cases, and only an additional attenuation factor takes care of the medium loss [6].

At last, it is important to mention that all the boundary extrapolation techniques presented above will affect the stability criteria of (3.42) which was derived without a consideration of radiation boundary condition. In particular, our computational experience indicates that the field extrapolation (5.6) or (5.7) requires the time step Δt to be reduced to:

$$\Delta t \leq (0.7 \sim 0.8) \times \frac{h}{c} \quad (5.11)$$

for stability.

Epilogue

Starting from the very simple concept of space-time computation of a one dimensional wave equation, we have presented the basic techniques and the associated theories of time domain numerical methods. The relations between discretization, computational procedures and stability have been discussed. Methods of initialization and termination of the computations and numerical treatments of dielectric interfaces have been presented. The method of "conforming boundary elements" and the "Poynting vector method" of simulating radiation conditions are recently developed by the authors. These techniques are quite essential in saving storage space and computing costs, which are especially important when the method is applied to large scale computations. We have used Gaussian primary fields rather than the often used step sinusoids in the illustrative results, because time sequence of the Gaussian results are more graphically presentable, and the CW results can really be obtained from their FFT's.

The one dimensional wave equation with dielectric interface has been successfully programmed by undergraduate students at the University of California for an IBM PC, and the results are displayed on CRT as they are computed. Indeed, time domain electromagnetics is a very effective method in providing physical insight to fields and waves, as well as a powerful computational technique for engineering applications.

References

- [1] K. S. Yee, "Numerical Solution of Initial Boundary Value Problems Involving Maxwell's Equations in Isotropic Media," *IEEE Trans. Ant. Prop.*, Vol. AP-14, pp. 302-307, May 1966.
- [2] C. L. Bennett and W. L. Weeks, "Transient Scattering from Conducting Cylinders," *IEEE Trans. Ant. Prop.*, Vol. AP-18, pp. 627-632, Sept. 1970.
- [3] K. S. Kunz and K. M. Lee, "A Three-Dimensional Finite-Difference Solution of the External Response of an Aircraft to a Complex Transient EM Environment: Part I - The Method and Its Implementation," *IEEE Trans. Electromagnetic Compatibility*, Vol. EMC-20, pp. 328-333, May 1978.
- [4] A. Taflove and M. E. Brodwin, "Numerical Solution of Steady-State Electromagnetic Scattering Problems Using the Time-Dependent Maxwell's Equations," *IEEE Trans. Microwave Theory Tech.*, Vol. MTT-23, pp. 623-630, Aug. 1975.
- [5] A. C. Cangellaris, C. C. Lin and K. K. Mei, "Point-Matched Time Domain Finite-Element Methods," National Radio Science Meeting, Boston, MA, June 1984.
- [6] C. C. Lin and K. K. Mei, "Time Domain Absorbing Boundary Condition in Lossy Media," *Int'l. IEEE/AP-S Symp.*, Boston, MA, June 1984.
- [7] J. A. Stratton, *Electromagnetic Theory*, McGraw Hill, New York, 1941.
- [8] K. H. Huebner, *The Finite-Element Method for Engineers*, John Wiley and Sons, New York, 1975.
- [9] S. Abarbanel and D. Gottlieb, "A Note on the Leap-Frog Scheme in Two and Three Dimensions," *J. Comp. Phys.*, Vol. 21, pp. 351-355, 1976.
- [10] S. H. Emerman, W. Schmidt and R. A. Stephen, "An Implicit Finite-Difference Formulation of the Elastic Wave Equation," *Geophysics*, Vol. 47, pp. 1521-

1526, Nov. 1982.

- [11] G. De Micheli and A. Sangiovanni-Vincentelli, "Characterization of Integration Algorithms for the Timing Analysis of MOS VLSI Circuits," *Circuit Th. and Applications*, Vol. 10, pp. 299-309, 1982.
- [12] C. D. Taylor, D. H. Lam and T. H. Shumpert, "Electromagnetic Pulse Scattering in Time-Varying Inhomogeneous Media," *IEEE Trans. Antennas and Propagation*, Vol. AP-17, pp. 585-589, Sept. 1969.
- [13] D. E. Merewether, "Transient Currents Induced on a Metallic Body of Revolution by an Electromagnetic Pulse," *IEEE Trans. Electromagnetic Compatibility*, Vol. EMC-13, pp. 41-45, May 1971.
- [14] A. Taflove, "Application of the Finite-Difference Time-Domain Method to Sinusoidal Steady-State Electromagnetic-Penetration Problems," *IEEE Trans. Electromagnetic Compatibility*, Vol. EMC-22, pp. 191-203, Aug. 1980.
- [15] R. Holland, L. Simpson, K. S. Kunz, "Finite-Difference Analysis of EMP Coupling to Lossy Dielectric Structures," *IEEE Trans. Electromagnetic Compatibility*, Vol. EMC-22, pp. 203-209, Aug. 1980.
- [16] O. C. Zienkiewicz, *The Finite Element Method in Eng. Science*, 2nd ed., McGraw-Hill, New York, 1971.
- [17] E. Oliveira, "Theoretical Foundations of the Finite Element Method," *Int. J. Solids Structures*, Vol. 4, pp. 929-952, 1968.
- [18] K. K. Mei, A. Cangellaris and D. J. Angelakos, "Conformal Time Domain Finite Difference Method," *Radio Science*, Vol. 19, pp 1145-1147, Sept.-Oct. 1984.
- [19] I. Ergatoudis, B. M. Irons and O. C. Zienkiewicz, "Curved Isoparametric, Quadrilateral Elements for Finite Element Analysis," *Int. J. Solids Structures*, Vol. 4, pp. 31-42, 1968.

- [20] E. L. Wachspress, *A Rational Finite Element Basis*, Academic Press Inc., New York, 1975.
- [21] J. F. Thompson, *Numerical Grid Generation*, Elsevier Science Publications, New York, 1982.
- [22] P. D. Lax, R. D. Richtmyer, "Survey of the Stability of Linear Finite Difference Equations," *Comm. Pure and Applied Math*, Vol. IX, pp. 267-293, 1956.
- [23] A. R. Mitchell and D. F. Griffiths, *The Finite Difference Method in Partial Differential Equations*, J. Wiley, New York, 1979.
- [24] J. C. Wilson, "Stability of Richtmyer Type Difference Schemes in Any Finite Number of Space Variables and Their Comparison with Multistep Strong Schemes," *J. Inst. Maths. Applics.*, Vol. 10, pp. 238-257, 1972.
- [25] R. Courant and D. Hilbert, *Methods of Mathematical Physics*, Interscience, New York, 1962.
- [26] B. Gustafsson, H.-O. Kreiss and A. Sundström, "Stability Theory of Difference Approximations for Mixed Initial Boundary Value Problems II," *Maths. of Comp.*, Vol. 26, pp. 649-686, 1972.
- [27] L. N. Trefethen, "Group Velocity Interpretation of the Stability Theory of Gustafsson, Kreiss and Sundström," *Journal of Computational Physics*, Vol. 49, pp. 199-217, 1983.
- [28] R. Vichnevetsky and J. Bowles, *Fourier Analysis of Numerical Approximations of Hyperbolic Equations*, SIAM, Philadelphia, 1982.
- [29] A. Sommerfeld, *Partial Differential Equations in Physics*, Academic Press, New York, 1949.
- [30] A. Arakawa and Y. Mintz, "The UCLA Atmospheric General Circulation Model," *UCLA Workshop Notes*, March-April 1974.

- [31] E. L. Lindman, "Free-Space Boundary Conditions for the Time Dependent Wave Equations," *J. Comp. Phys.*, Vol. 18, pp. 66-78, 1975.
- [32] A. C. Reynolds, "Boundary Conditions for the Numerical Solution of Wave Propagation Problems," *Geophysics*, Vol. 43, pp. 1099-1110, Oct. 1978.
- [33] B. Engquist and A. Majda, "Radiation Boundary Conditions for Acoustic and Elastic Wave Calculations," *Comm. Pure Appl. Math.*, Vol. 32, pp. 313-357, 1979.
- [34] G. Mur, "Absorbing Boundary Conditions for Finite-Difference Approximation of the Time-Domain Electromagnetic-Field Equations," *IEEE Trans. Electromagnetic Compatibility*, Vol. EMC-23, pp. 1073-1077, Nov. 1981.
- [35] A. Bayliss and E. Turkel, "Radiation Boundary Conditions for Wave-Like Equations," *Comm. Pure Appl. Math.*, Vol. 33, pp 707-725, 1980.
- [36] R. W. Ziolkowski, N. K. Madsen and R. C. Carpenter, "Three-Dimensional Computer Modeling of Electromagnetic Fields: A Global Lookback Lattice Truncation Scheme," *J. Comp. Phys.*, Vol. 50, pp. 360-408, June 1983.
- [37] D. Gottlieb and E. Turkel, "Boundary Conditions for Multistep Finite-Difference Method for Time Dependent Equations," *J. Comp. Phys.*, Vol. 26, pp. 181-196, 1978.
- [38] F. G. Friedlander, "On the Radiation Field of Pulse Solutions of the Wave Equation," *Proc. Royal Society of London, Ser. A*, Vol. 269, pp. 53-65, 1962.
- [39] Van Bladel, *Electromagnetic Fields*, McGraw-Hill, New York, 1964.

Figure Captions

- Fig. 2.1 One-dimensional hyperbolic problem.
- Fig. 2.2 Discretization of solution domain D .
- Fig. 2.3a Plane wave reflection from perfectly conducting wall.
- Fig. 2.3b Plane wave reflection and transmission at dielectric interface.
- Fig. 2.3c Plane wave propagation through radiation boundary.
- Fig. 2.4 Piece-wise linear approximation using tent functions.
- Fig. 2.5 Tent function as a basis.
- Fig. 3.1 E_z case scattering by an infinite circular cylinder.
- Fig. 3.2 Time-domain finite-difference mesh for circular cylinder.
- Fig. 3.3 Finite-element representation of circular cylinder.
- Fig. 3.4 Two-dimensional interpolation: (a) basis function $\varphi_i(\bar{r})$; (b) field representation within a quadrilateral element.
- Fig. 3.5 Two complementary grids for electric and magnetic fields.
- Fig. 3.6 Arbitrary quadrilateral.
- Fig. 3.7 The unit square on $\xi-\eta$ plane is mapped through $\{\Phi\}$ to a quadrilateral on the x-y plane.
- Fig. 3.8 An almost degenerate quadrilateral.
- Fig. 3.9 Grid generation by mapping.
- Fig. 3.10 Grid generation using an averaging procedure.
- Fig. 3.11 The intersections of a rectangular grid with the body contour create boundary elements.
- Fig. 3.12 Inappropriate boundary elements.

- Fig. 3.13 Appropriate boundary elements.
- Fig. 3.14 Computation of the normal component of the electric field on the scatterer surface.
- Fig. 3.15 Gaussian pulse: $g(t)=e^{-t^2/T^2}$.
- Fig. 3.16 Polar diagram of C^*/C .
- Fig. 3.17 Computation of the magnetic field inside an electric element that contains the dielectric interface.
- Fig. 3.18 Computation of the electric field inside a magnetic element that contains the dielectric interface.
- Fig. 3.19 Discontinuity in normal derivative of H_z .
- Fig. 3.20 Maxwell's "Fish-Eye" lens.
- Fig. 3.21 Wave focusing by a fish-eye lens.
- Fig. 4.1 General hexahedron element.
- Fig. 5.1 Illustration of Bayliss and Turkel's radiation boundary condition.
- Fig. 5.2 Field extrapolation according to B_1 .
- Fig. 5.3 Ratio between the sizes of modeled object and the computational domain.
- Fig. 5.4 Global Poynting vector \bar{S} as a result of superposition of fields produced by a distributed source.
- Fig. 5.5 Poynting vector resulting from a superposition of fields due to two line sources.

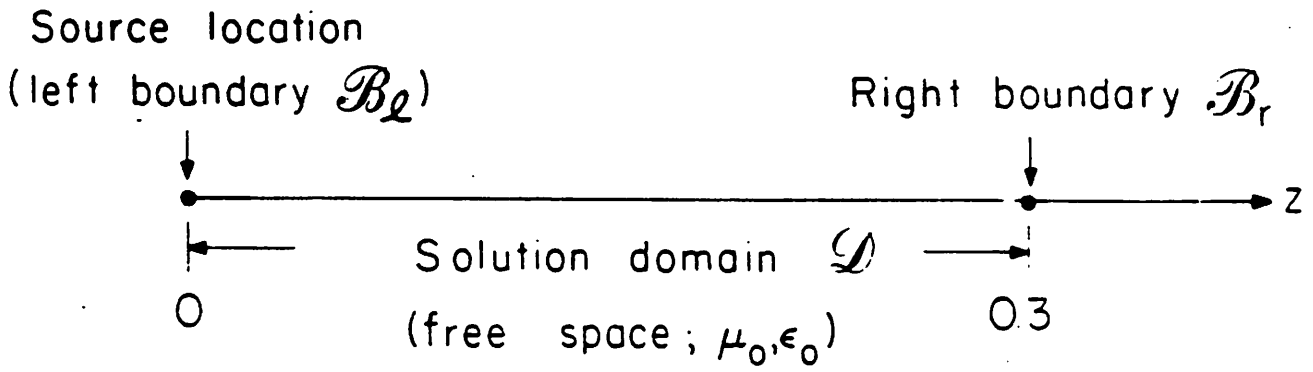


Fig. 2.1

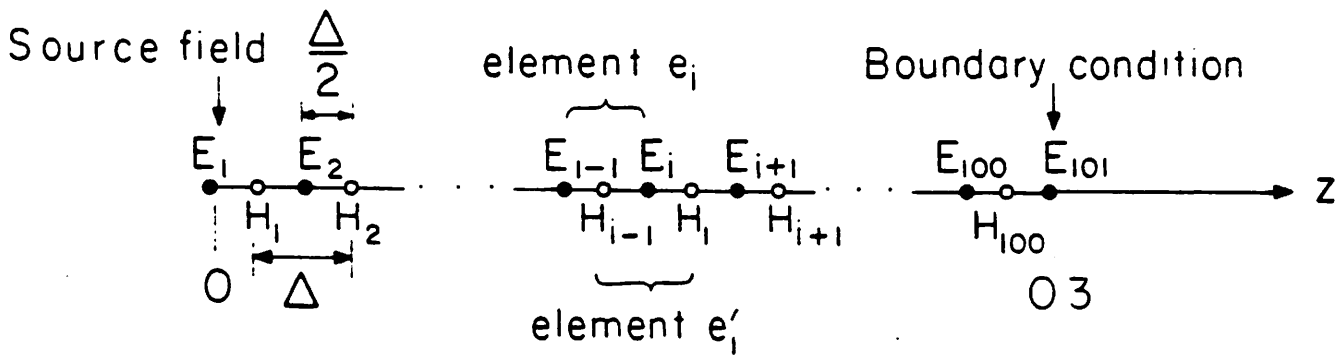


Fig. 2.2

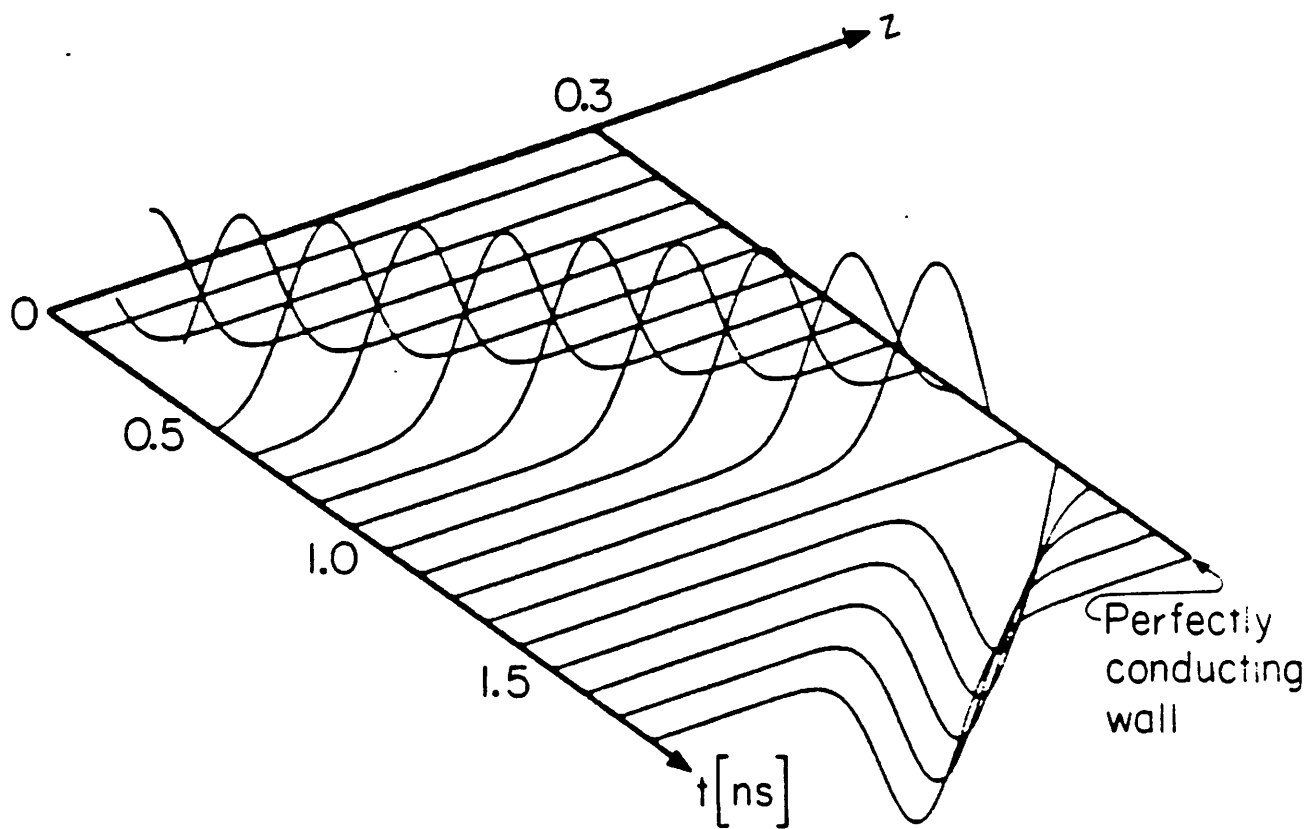


Fig. 2.3 a

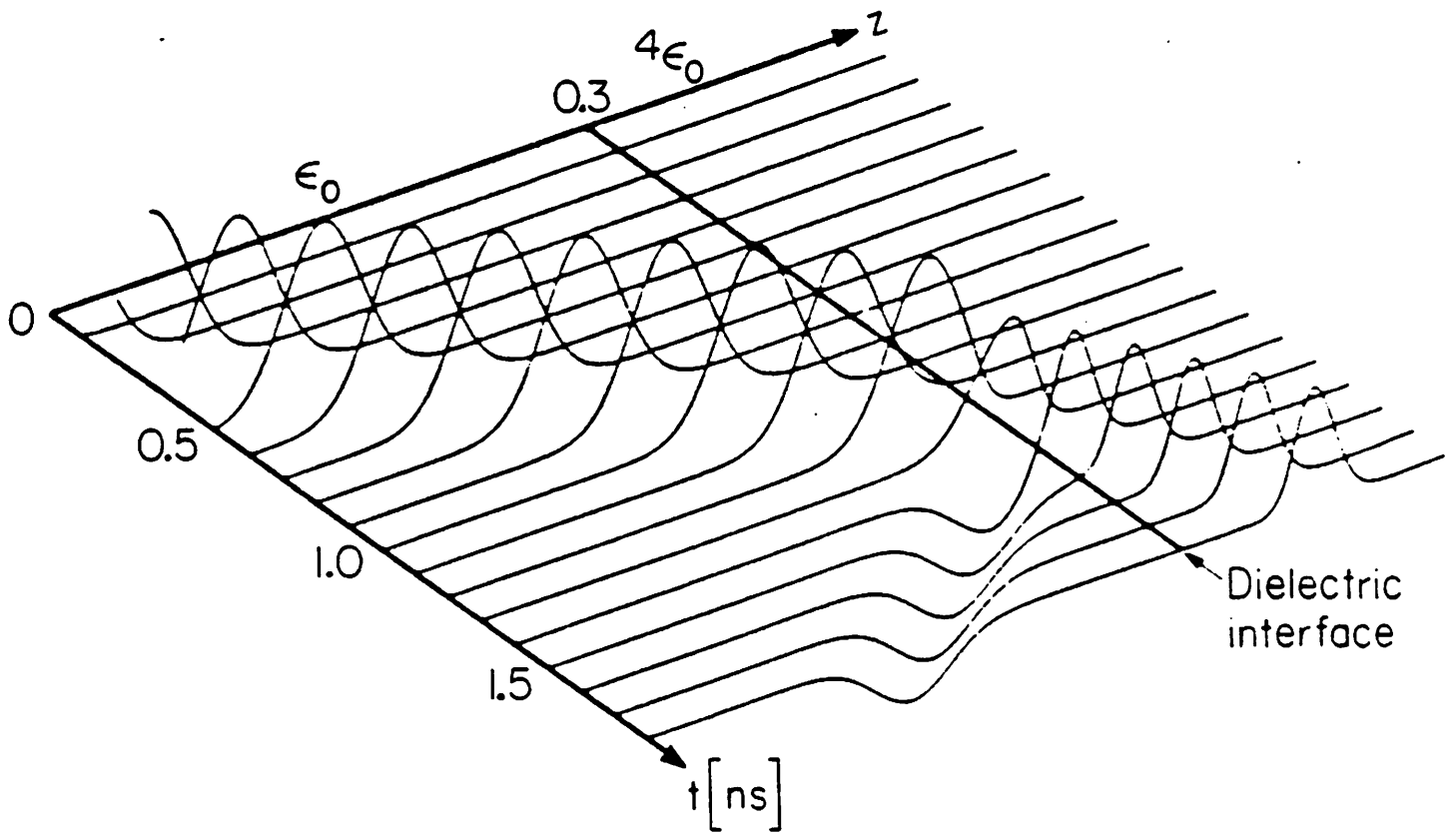


Fig. 2.3b

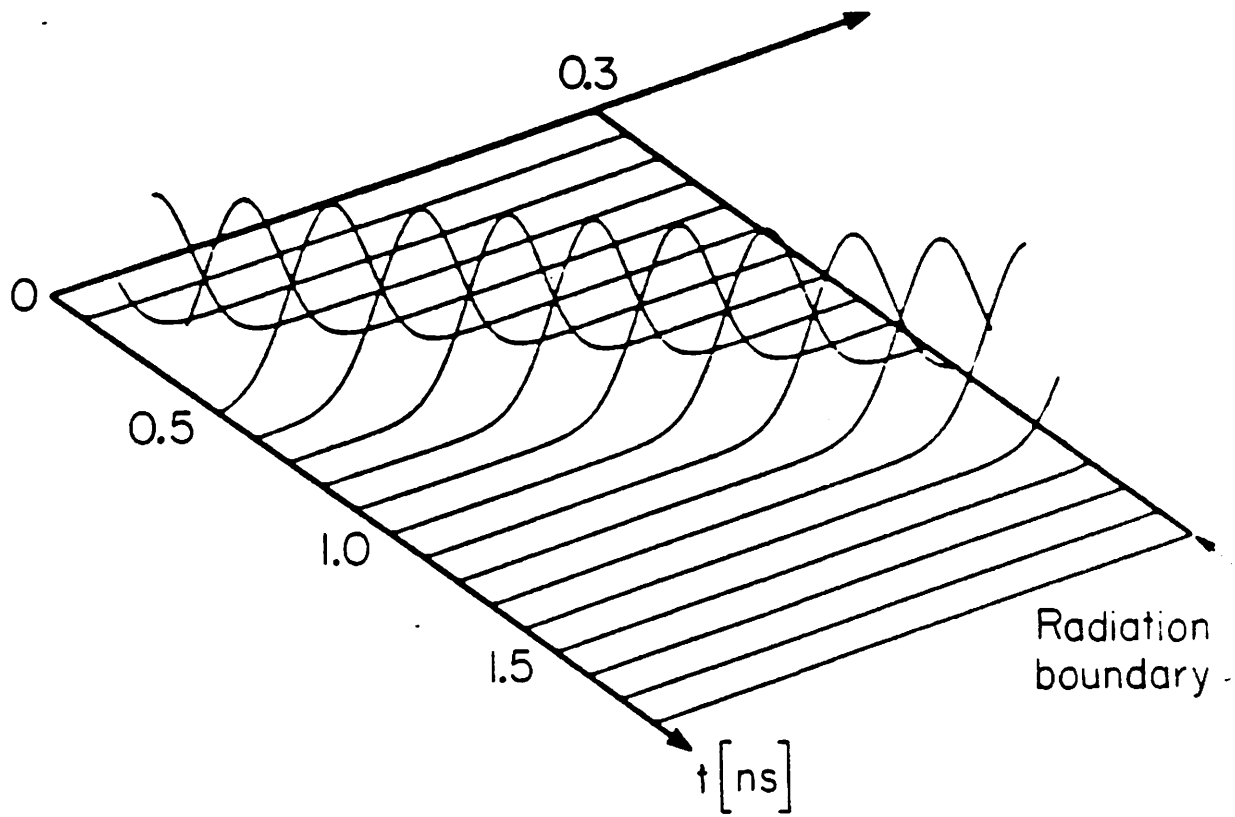


Fig. 2.3c

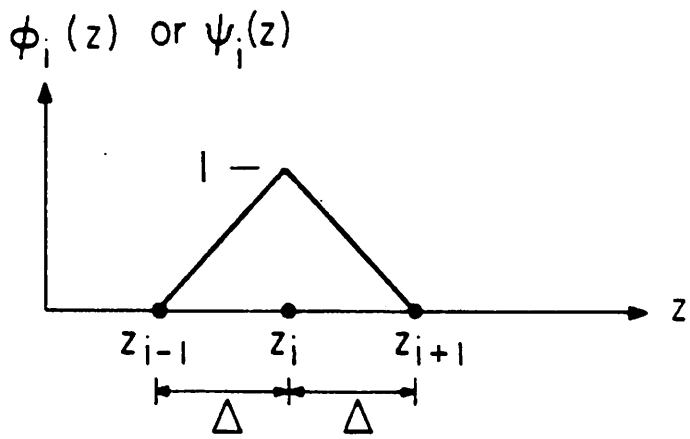


Fig. 2.5

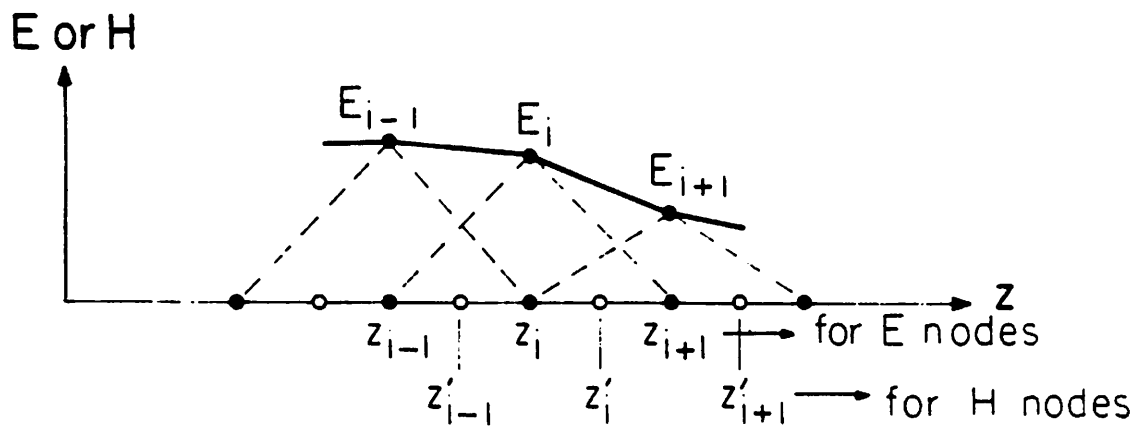


Fig. 2.4

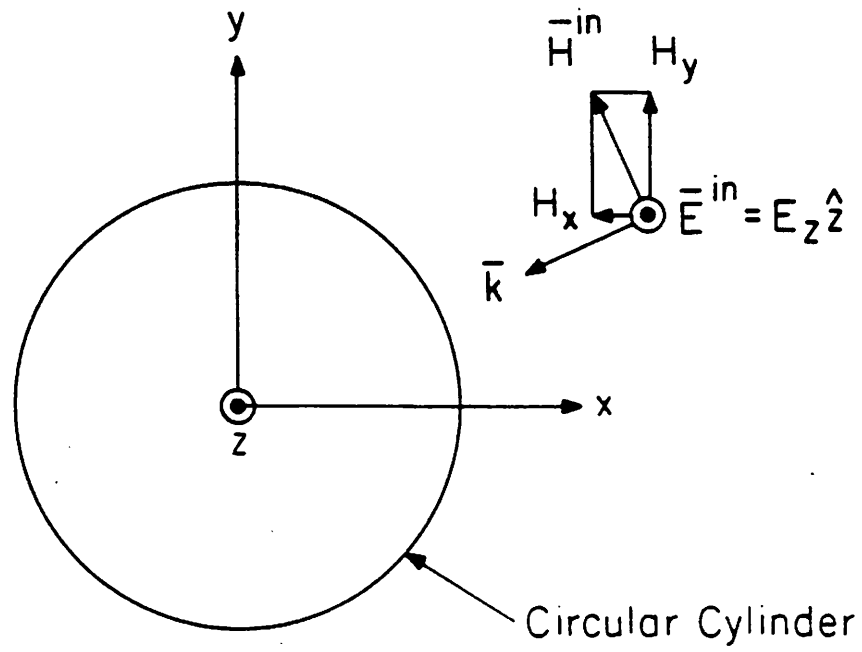


Fig. 3.1

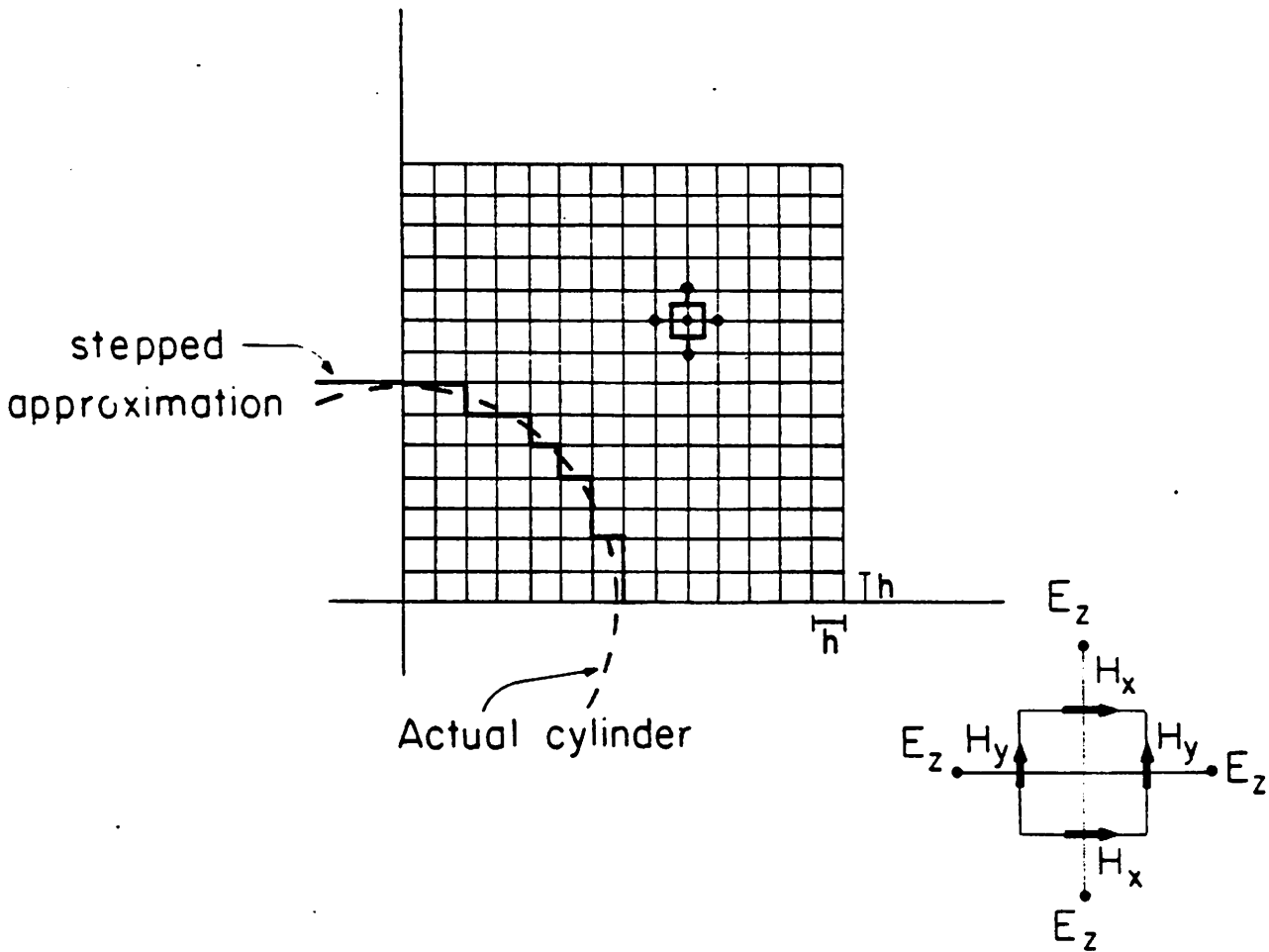


Fig. 3.2

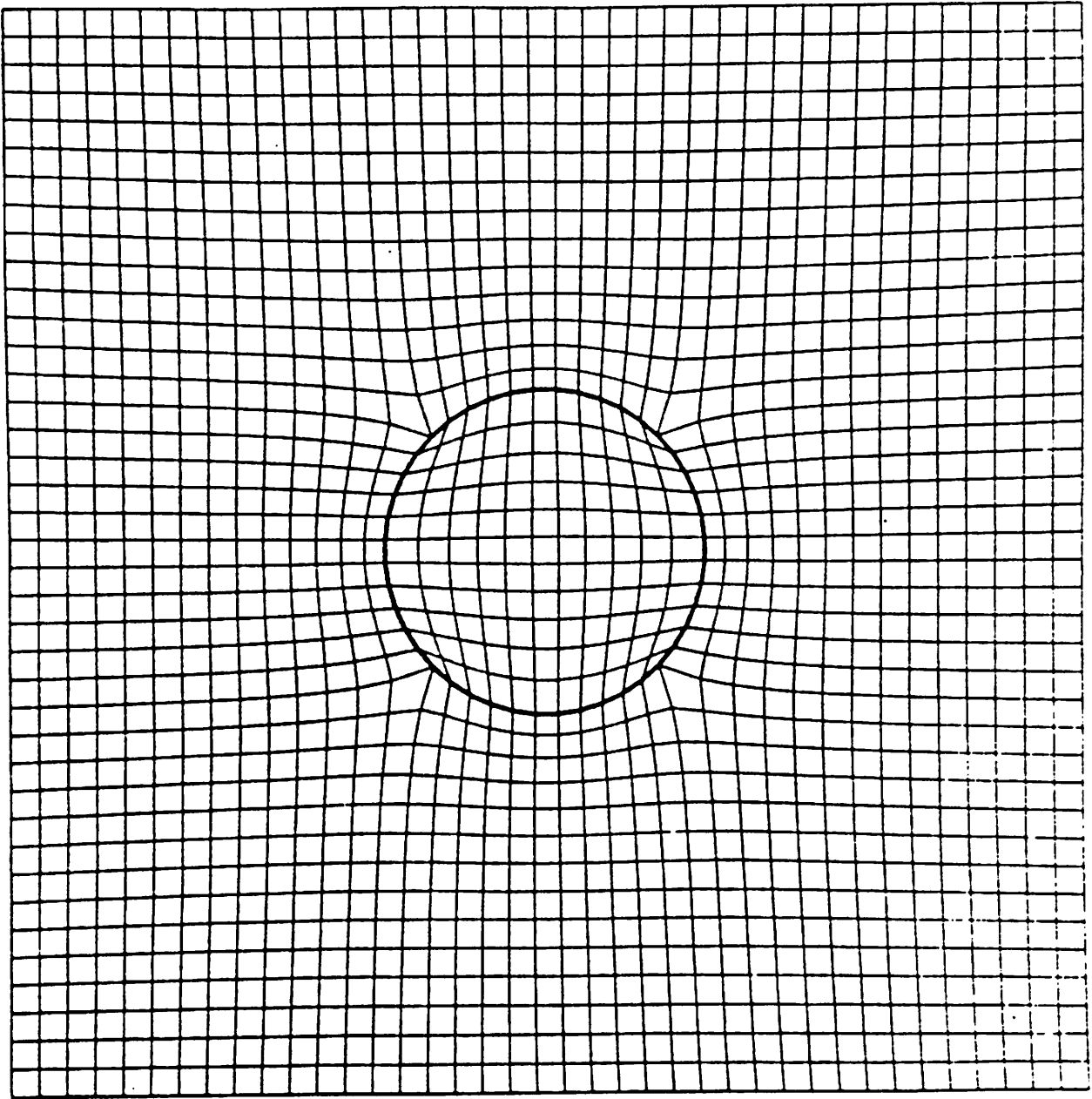


Fig. 3.3

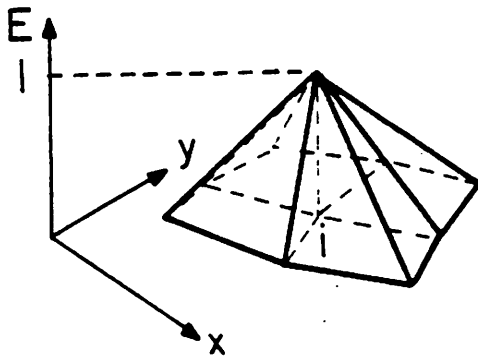


Fig. 3.4 a

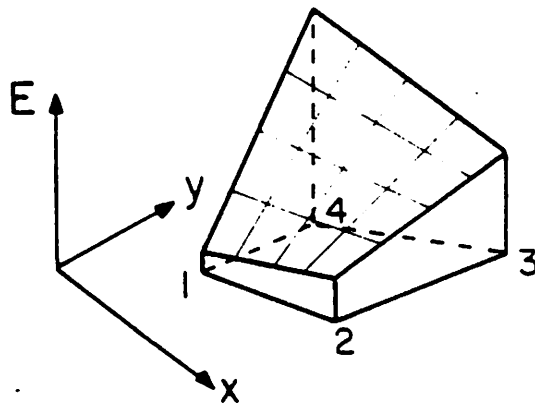


Fig. 3.4 b

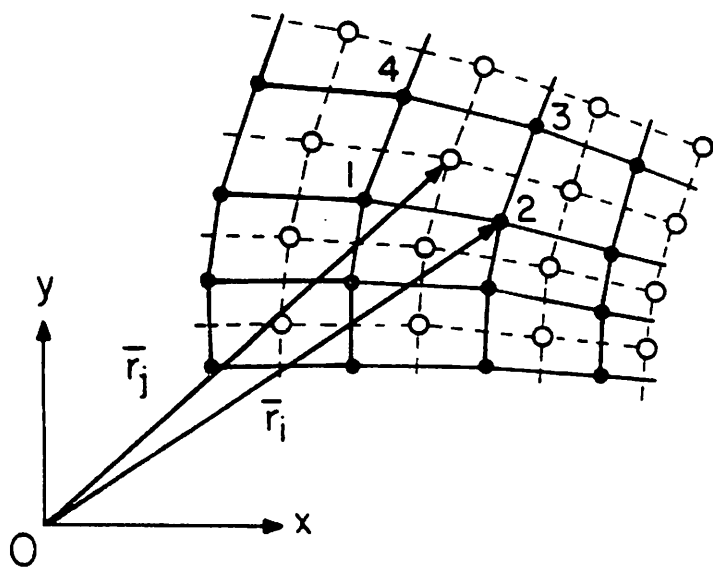


Fig. 3.5

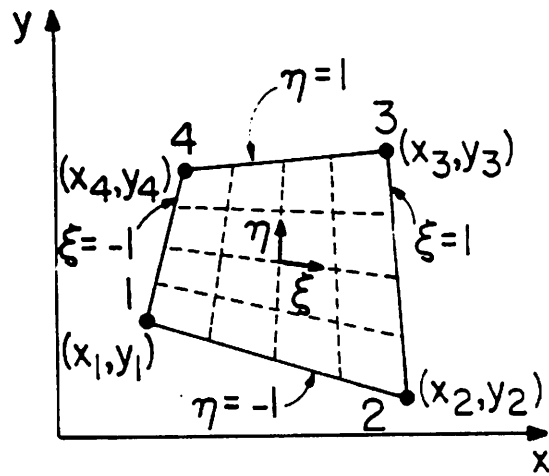


Fig. 3.6

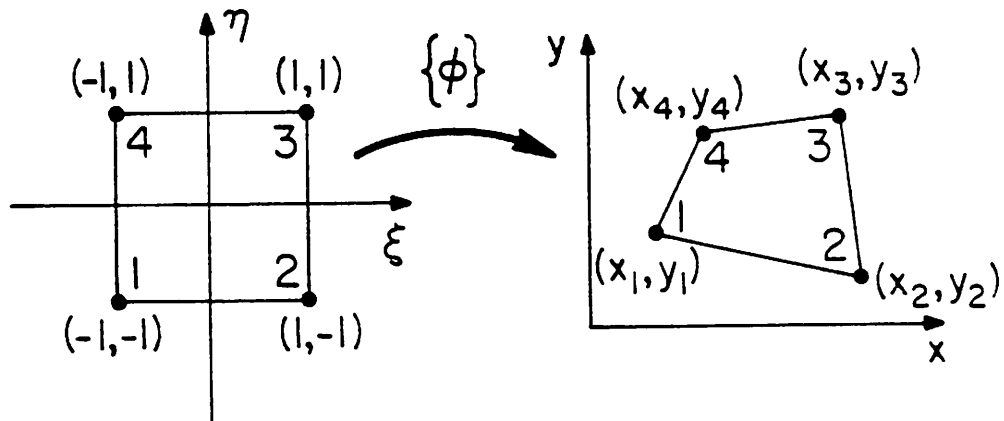


Fig. 3.7

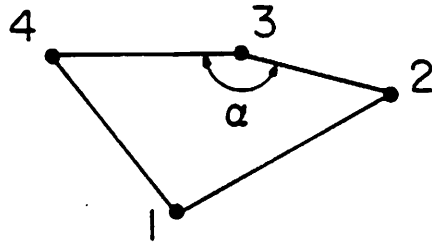


Fig. 3.8

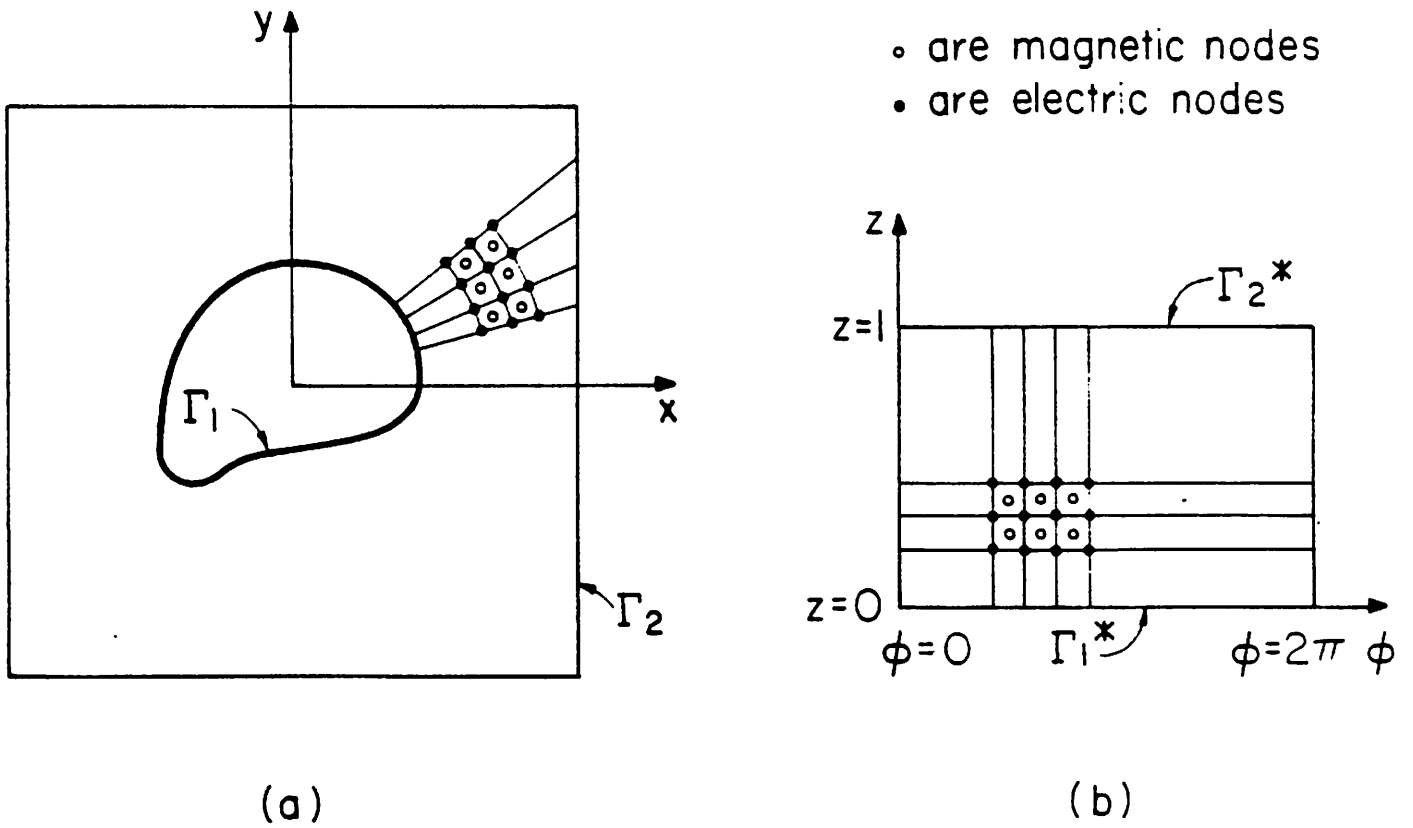


Fig. 3.9

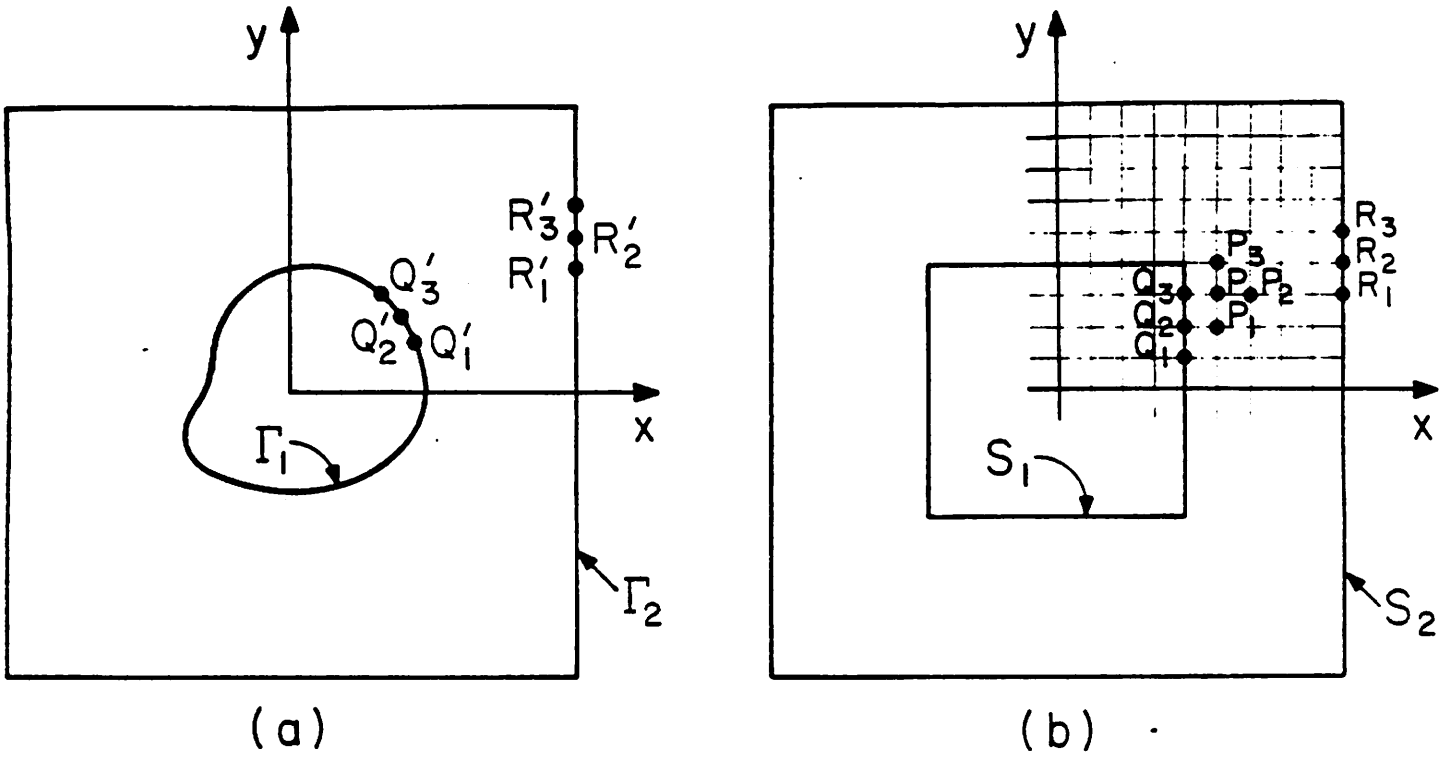


Fig. 3.10

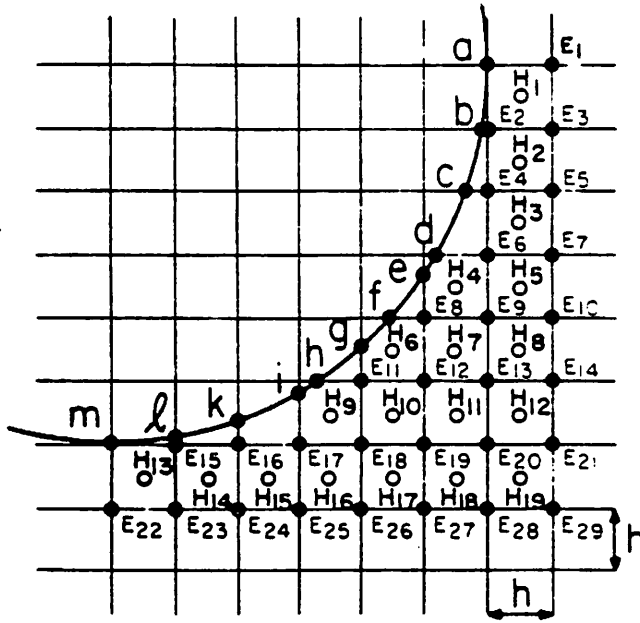
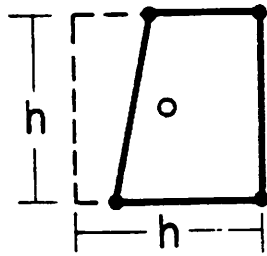
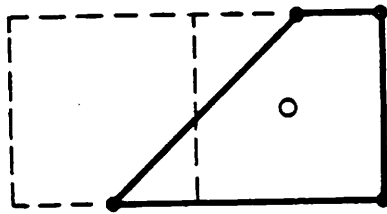


Fig. 3.11

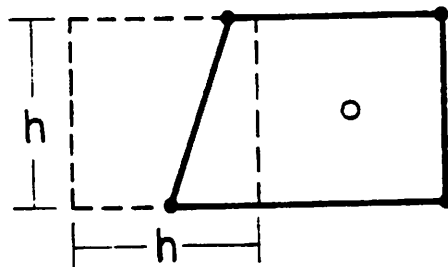


(a)

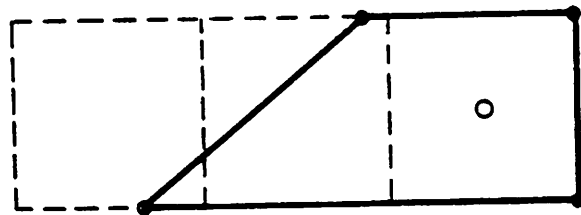


(b)

Fig. 3.12



(a)



(b)

Fig. 3.13

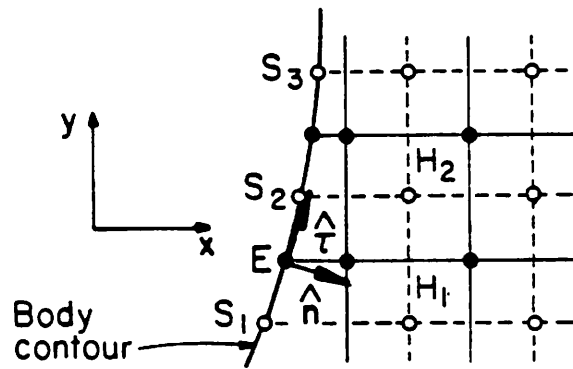


Fig. 3.14

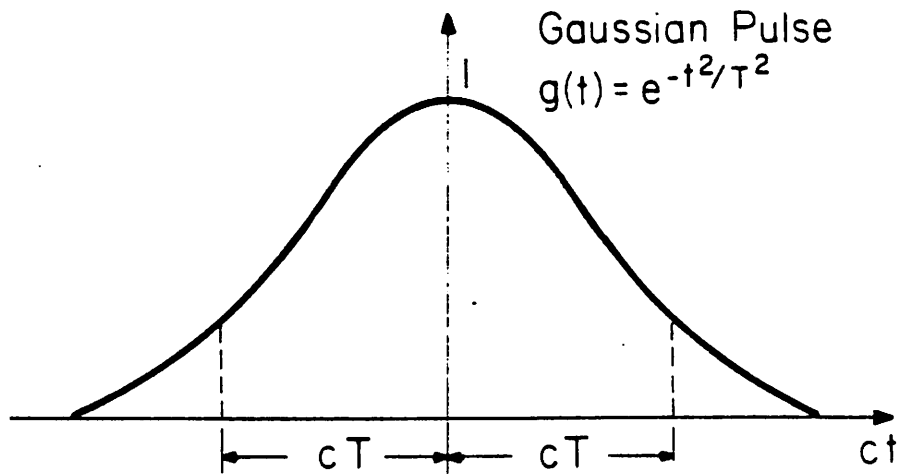


Fig. 3.15

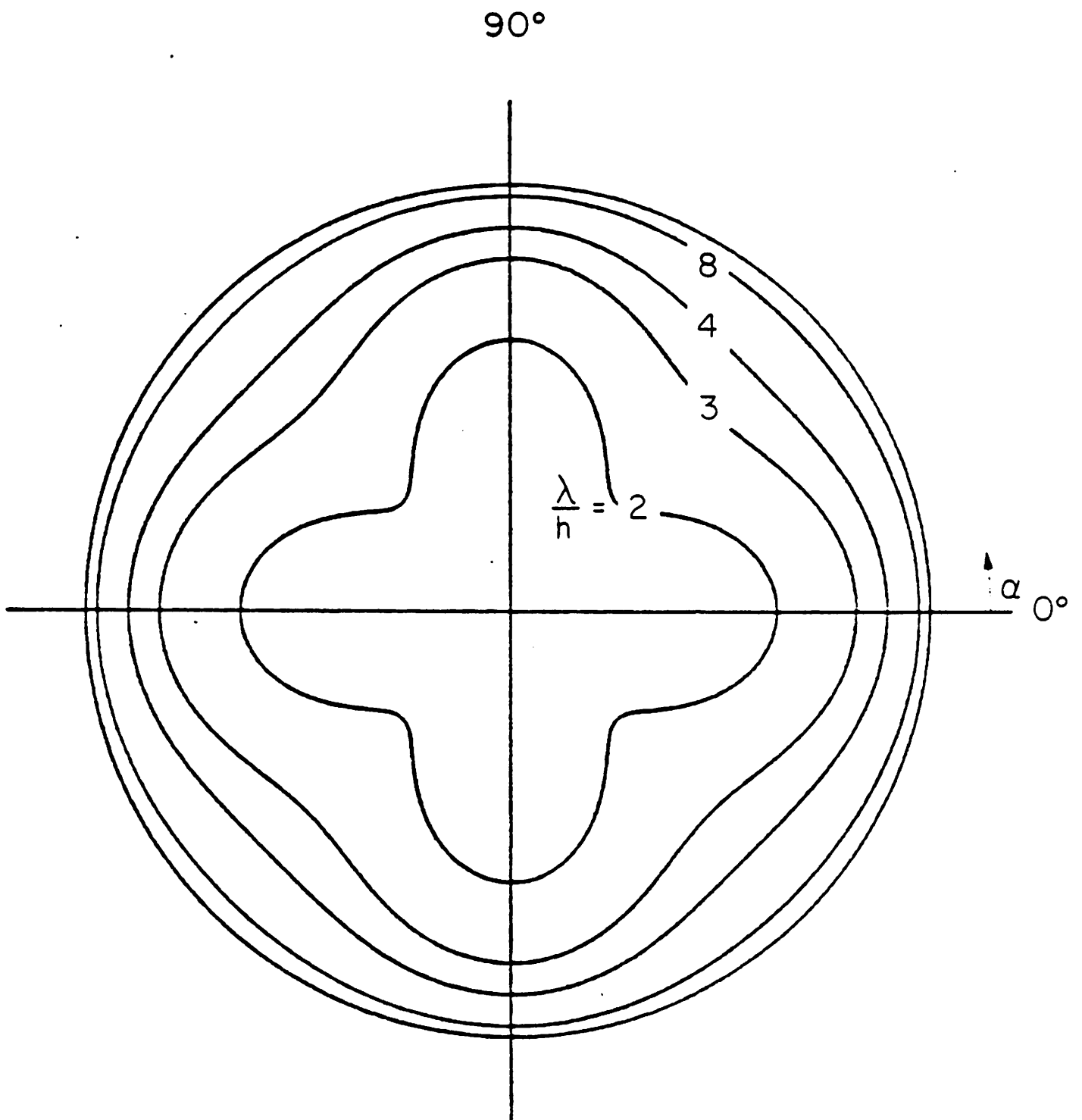


Fig. 3.16

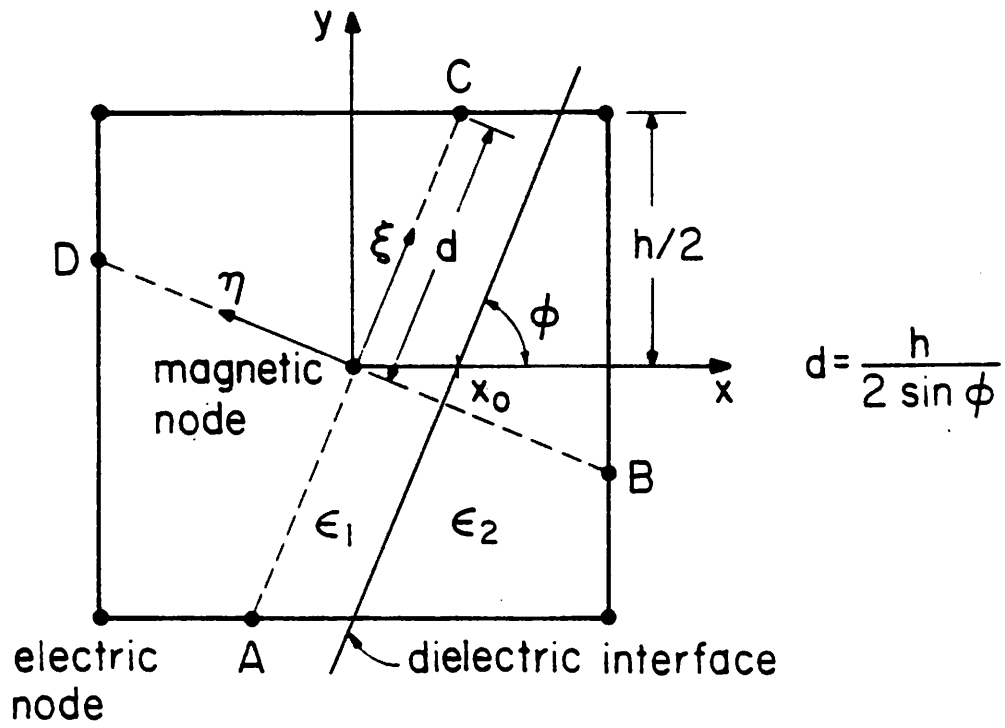


Fig. 3.17

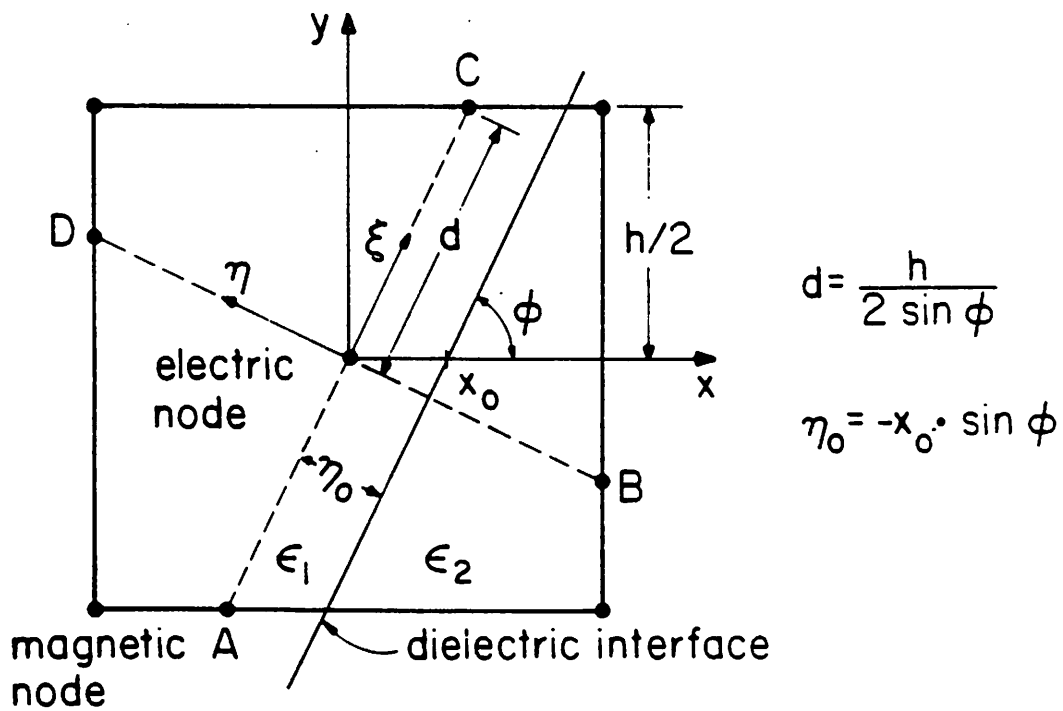
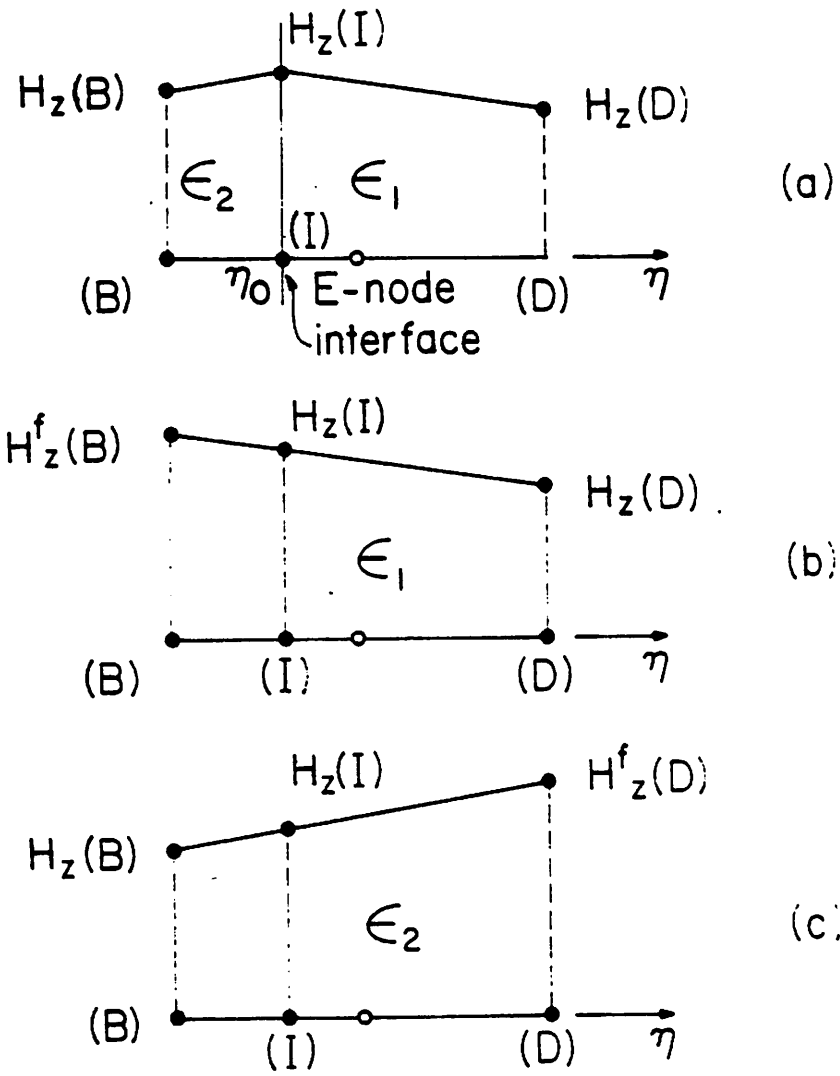
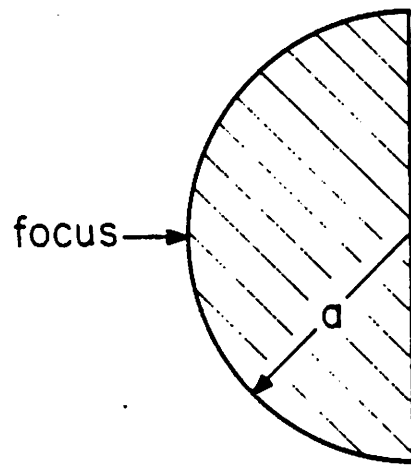


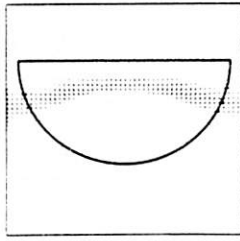
Fig. 3.18



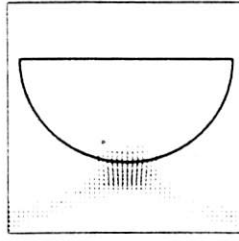


$$\epsilon_R = \frac{4}{[1+(r/a)^2]^2}$$

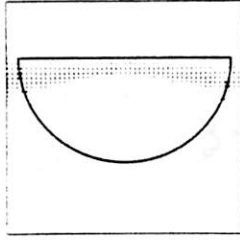
Fig. 3.20



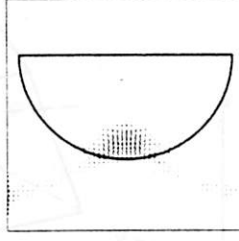
4



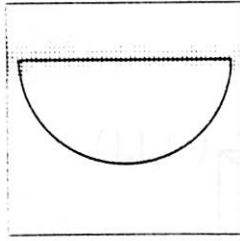
9



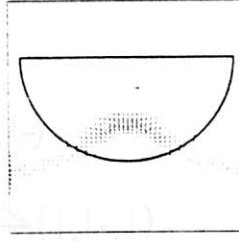
3



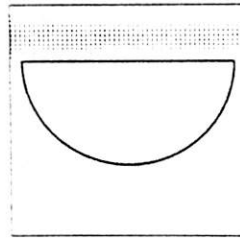
8



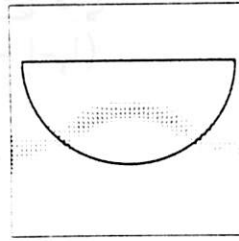
2



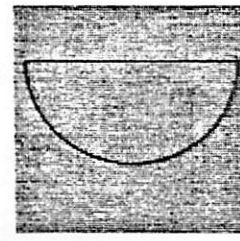
7



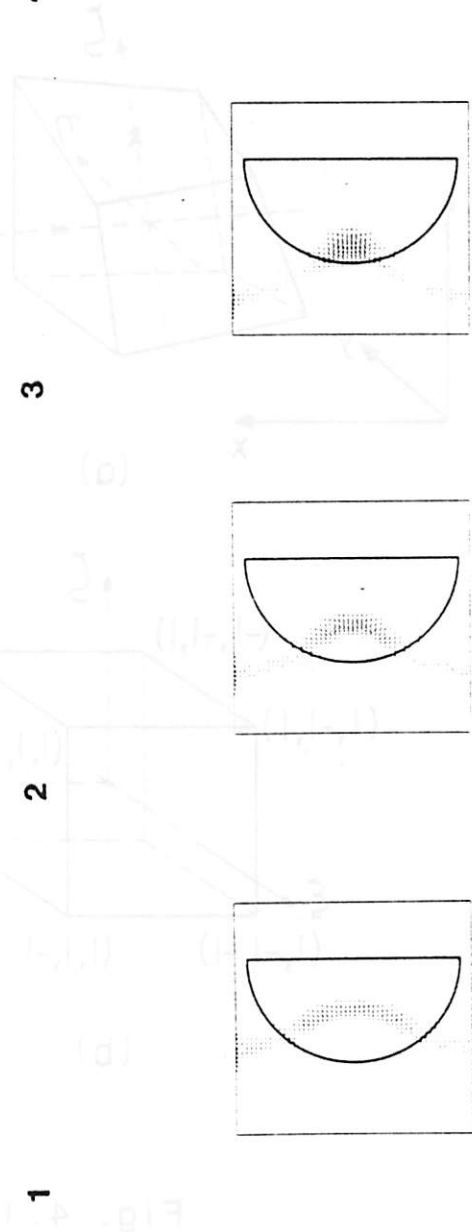
1



6



5



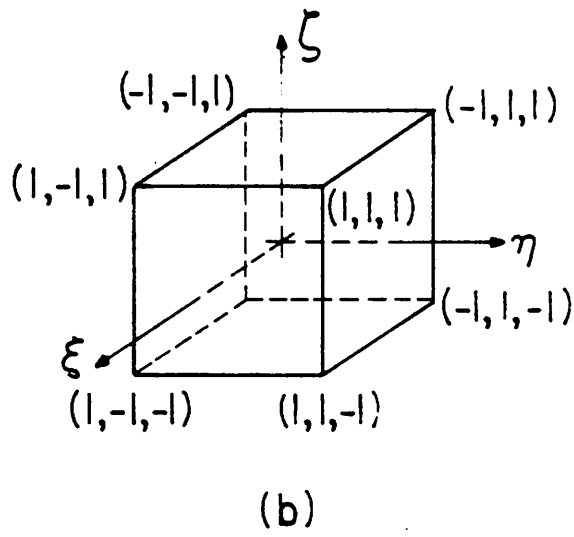
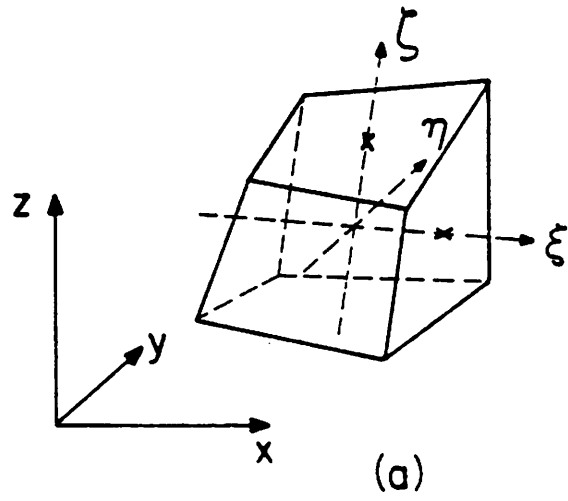
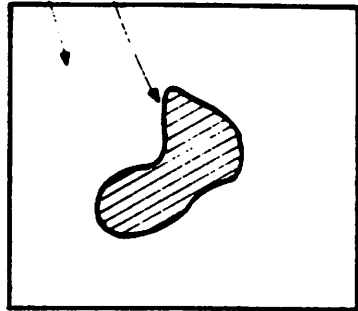


Fig. 4.1

Numerical solution region \mathcal{D}

Source or scatterer



Radiation boundary ;
 $B_m =$ field continuity with
 m first terms

Outer region; $u^{sc} \approx \sum_{i=1}^m \frac{f_i(t - \frac{r}{c}, \theta, \phi)}{r^i}$

Fig. 5.1

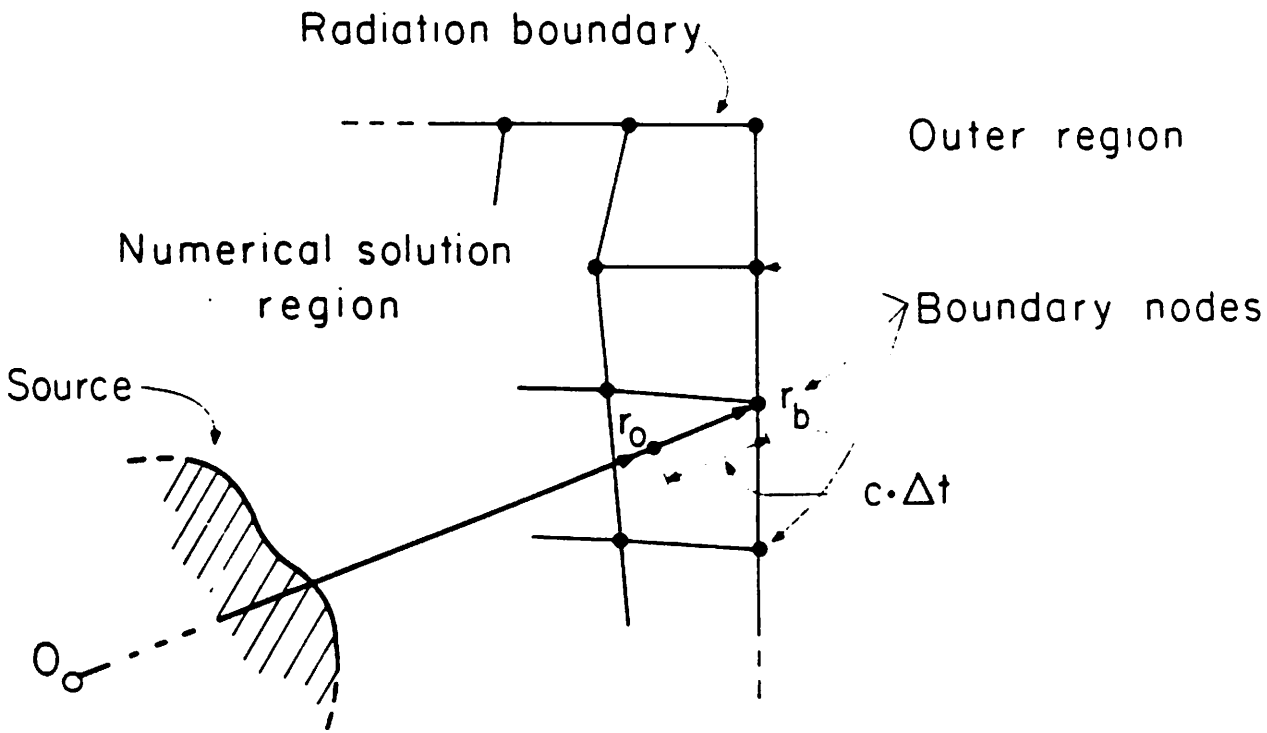
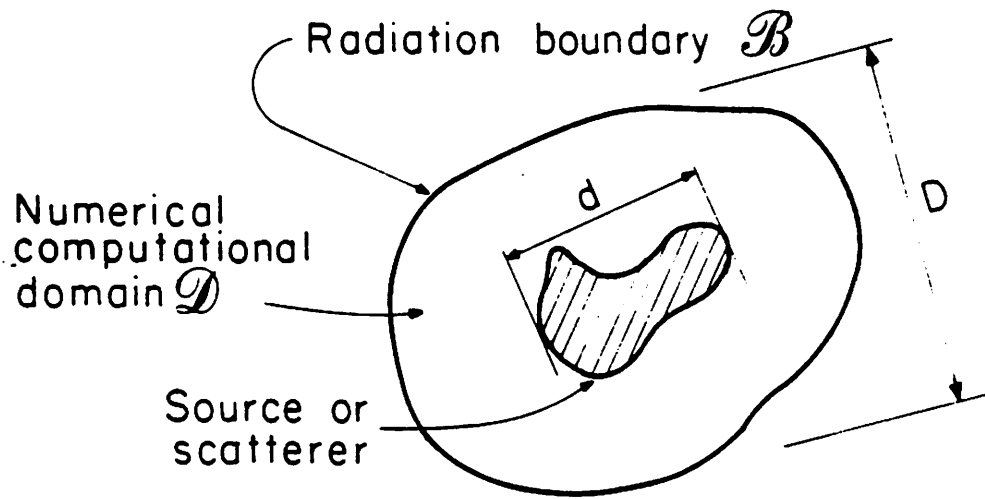


Fig. 5.2



$\left\{ \begin{array}{l} d; \text{ maximum dimension of the source or the scatterer} \\ D; \text{ minimum distance across the computational domain} \end{array} \right.$

Fig. 5.3

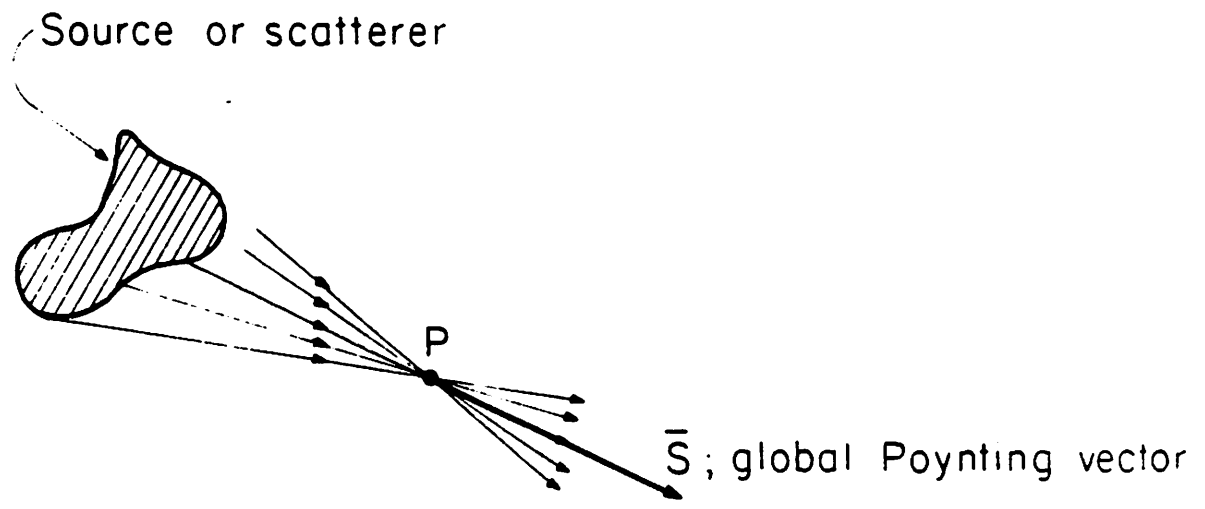
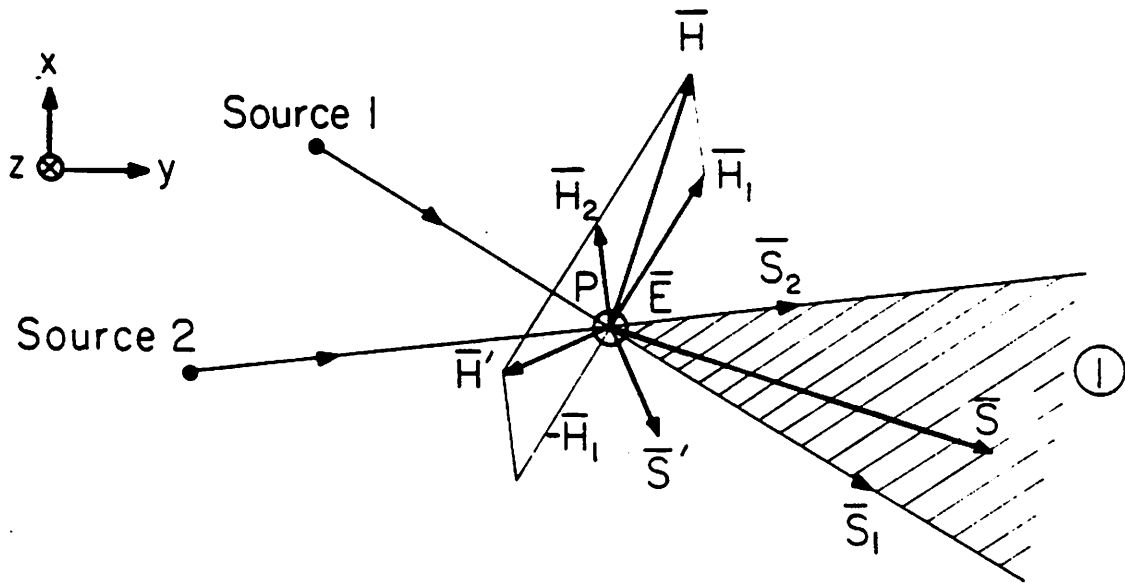


Fig. 5.4

$$\vec{E}_1 = E_1 \hat{z}$$

$$\vec{E}_2 = E_2 \hat{z}$$



- \vec{H} ; total magnetic field when E_1 and E_2 are of same polarity
- \vec{H}' ; total magnetic field when E_1 and E_2 are of opposite polarity
- \vec{S} ; total Poynting vector when E_1 and E_2 are of same polarity
- \vec{S}' ; total Poynting vector when E_1 and E_2 are of opposite polarity

Fig. 5.5